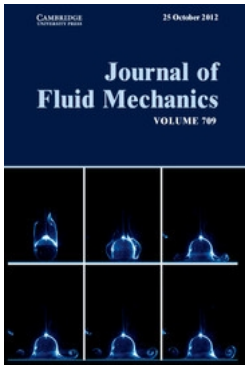

Theoretical prediction and design for vortex generators in turbulent boundary layers

F. T. Smith

Journal of Fluid Mechanics / Volume 270 / July 1994, pp 91 - 132
DOI: 10.1017/S0022112094004210, Published online: 26 April 2006

J. Fluid Mech. (1994), *vol.* 270, *pp.* 91–131

Theoretical prediction and design for vortex generators in turbulent boundary layers

By F. T. SMITH

Department of Mathematics, University College London, Gower Street, London WC1E 6BT, UK

(Received 6 March 1993 and in revised form 20 December 1993)

A theoretical study is presented of three-dimensional turbulent flow provoked in a boundary layer by an array of low-profile vortex generators (VGs) on the surface. The typical VG sits in the logarithmic region of the incident boundary layer, and the turbulence model used seems representative in this region. The governing equations yield a forward-marching three-dimensional vortex-type system, which is solved computationally and analytically for spanwise periodic VG arrays. Streamwise vortex patterns of various strengths are produced downstream, owing to three-dimensional distortion of the original logarithmic profile and to the turbulent stresses present. Predictions are given for certain basic VG shapes, e.g. triangular, with various spanwise spacings, and the predictions are found to agree favourably overall with recent experiments. In addition, the analytical formulae obtained prove useful in suggesting designs for favourable VG distributions, based on three factors: close spanwise packing, increased VG length, and suitably non-smooth spanwise shaping.

1. Introduction

Vortex generators (VGs), inserted in a boundary layer, can produce such significant effects in the flow performance downstream that they have been and continue to be of much experimental interest (Pearcey 1961; McCormick 1992; Freestone 1991/2; see also Schubauer & Spangenberg 1960). Various sizes, shapes and distributions of VGs have been examined experimentally, under various flow conditions. Some favourable VG configurations and effects have been found from such studies, notably Pearcey (1961), McCormick (1992) and references therein. 'Favourable' refers, for example, to the desired property of reducing or eliminating separation in the flow downstream, say in a shock/boundary-layer interaction (McCormick 1992), along with a minimal drag penalty from the VG itself. A definite pattern for the choice of a favourable VG in given flow conditions seems unclear as yet, however. The present work is a theoretical attempt to address VG effects systematically, for a turbulent boundary layer. Some helpful modelling has been done previously, mainly of an inviscid nature and notably in Pearcey (1961), Freestone (1991/2), Mounts & Barber (1992) and references therein. Yet there appears to be little or no systematic theory and parameter investigation to date especially in the most common practical context of turbulent boundary layers. Such an investigation, into the parametric dependence and the scaling laws, could prove very beneficial with regard not only to predictions for given VG arrays but also to the practical design problem, in view of the large number of geometric and flow parameters present.

Many basic questions arise directly from the experimental findings. For example, is the precise VG shape vital, or an overall property of the shape? Are sharp edges on the

VGs advantageous? Is flow separation, at the VGs, essential to a favourable effect downstream? Is streamwise momentum transferred to the wall or off the wall, and which, if either, is beneficial? What are the effects on the displacement and shape factor downstream, and are these major factors in determining the success or failure of a VG system? Some of these issues are tackled below. Further, the original boundary layer, ahead of the VGs (or in their absence), is *turbulent* in most real cases, including the cases of interest here, and so the relevance of laminar-flow theory is lost or limited. Along with that, the VG influence is definitely a *three-dimensional* one, associated with the creation of streamwise vortex flows downstream. Hence we are led to tackle three-dimensional turbulent flows in a boundary layer. As indicated above, there are many parameters indeed, including at least 5–6 lengthscales (3 for the VG, 2–3 for the original boundary layer) apart from the actual variation of the VG shape. So here the intention is to identify main parameters and their effects, and to gain insight into the influences of VG shape, size, spacing, orientation, stagger, etc., and the various scales involved. This is meant to be complementary to computational studies of VG flows (e.g. Mounts & Barber 1992; Esmaili & Piomelli 1992), some of which are in progress. Thus we aim at general formulae as much as possible, for instance for the displacement and the streamwise velocity and vorticity generated downstream of a VG array, in terms of the VG shapes and distributions. This is found to be feasible in principle.

The present theoretical research arose in particular from the experimental studies at United Technologies Research Center on *low-profile* VGs. The theory below assumes that the typical VG involved (see figure 1) is slender, of relatively low profile, with its characteristic spanwise lengthscale being comparable with the oncoming boundary-layer thickness, and the global Reynolds number Re is large. These assumptions, which are made more specific in §2, seem in line with the experimental arrangements. As a result, the governing equations reduce to a forward-marching three-dimensional vortex system, allowing relatively fast accurate computation and theoretical analysis (in §3, where a linearized system is obtained, in §§4 and 5, which address single-mode VGs, and then in §6, which is concerned with realistic VG shapes and arrays). A representative time-mean turbulence model is used (see §§ 2 and 3), namely the Cebeci–Smith one but extended into the current three-dimensional context; other models for three-dimensional flows are considered in Chima & Yokota (1989), Vatsa & Wedan (1988), Degani, Smith & Walker (1992), Cebeci & Smith (1974). The applicability and 'workability' of this model are discussed elsewhere (Degani *et al.* 1992; Neish & Smith 1988, 1992) for a variety of configurations. In addition, however, the model is felt likely to be increasingly appropriate for the current low-profile VGs anyway, where most of the VG-generated flow effects occur at first in the logarithmic part of the boundary layer (the significance of which is addressed in the next paragraph). For this turbulent flow context, which proves to be more analyzable (as in Degani *et al.* 1992; Neish & Smith 1988, 1992) than the corresponding one for laminar flow, there appears to be no other such theoretical work. Again, we observe that some of the research applies also to high-profile VGs.

The vortex system studied here concerns relatively long-scale behaviour. Shorter-scale behaviour is associated mainly with the three-dimensional Euler system, apart from the effects of separation from the VG. Here separation can be allowed, in the formulation set out in §2 below, but we choose instead to focus on other features first, including those concerning parameters and scales mentioned previously, by examining a linearized version for low VGs. This raises the possibility that separation at the VG itself is not a vital ingredient in the success of a VG distribution. Instead, a favourable vortex pattern is found to be produced (e.g. see §§6 and 7), downstream of the VG,

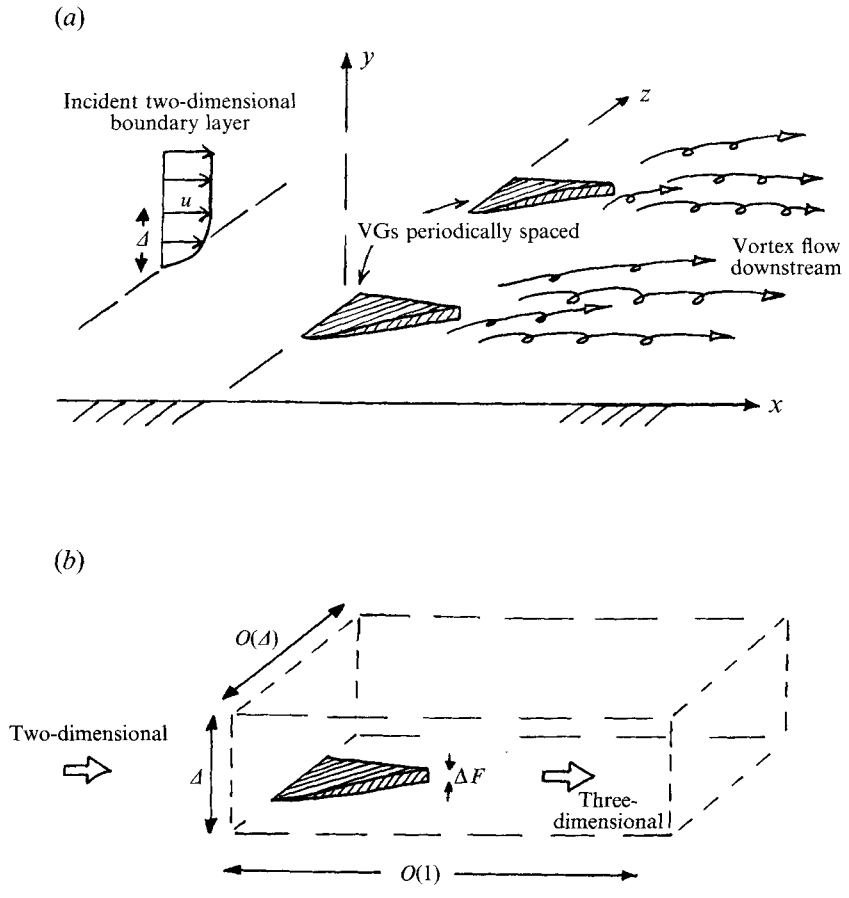

FIGURE 1. Sketch of flow structure: (*a*) general, (*b*) lengthscales.

owing partly to the three-dimensional distortion of the strong vorticity that is present in the oncoming logarithmic profile and partly to the action of the turbulent stresses; this agrees with a referee's comment that the direction of the vorticity vector is tilted away from the spanwise direction as a result of the surface irregularity (the VG).

Further points are presented in §7, which includes in particular recommendations on VG shapes and arrays. Certain other aspects, including alternative turbulence models and cross-flow and compressibility effects, can be examined in later studies of course. We note also that helpful discussions with D. McCormick, J. Mounts and T. Barber tended to suggest a combination of small profile drag with strong streamwise vorticity production and displacement effects as a measure of success for the VG distribution; here we focus on the streamwise vorticity and displacement (see §§6 and 7). Again, Fourier decomposition is used (§§3–6) to deal with the linearized system mentioned above. Realistic VG shapes are then accommodated (in §6) by superimposing the Fourier components, firstly to yield predictions for triangular and other planforms of VG (these predictions are found to compare favourably overall with recent experiments, as shown in Appendix C) and secondly to help design favourable VG shapes and distributions. The latter aspect is emphasized in §7.

The characteristic length and velocity are taken to be the maximum dimension l^* of the typical VG and the typical free-stream velocity u_∞^* near the VG, respectively. As a

starting point, the incompressible regime is studied here, with the fluid density being ρ^*, and with the oncoming boundary layer being two-dimensional, although the main application areas are more in the transonic regime with cross-flow. The wall friction velocity is denoted by u_τ^*, which is of the order of u_∞^* $(\ln Re)^{-1}$ at large Re, and the oncoming boundary layer is then two-tiered (Bush & Fendell 1972; Mellor 1972; Cebeci & Smith 1974; Degani *et al.* 1992; Neish & Smith 1988, 1992).

The main findings of the research so far, then, are contained essentially in §§6 and 7 below (along with the parameter groupings and comparisons in Appendix C). Section 6, concerning real VG shapes, provides numerical predictions for triangular VGs and smoothed VGs for various spanwise packings, among other things, followed by theoretical analysis for general distributions, and comments on the results produced. Section 7 then turns more to the design aspect, based on the computations and theoretical analysis of §6. Specific recommendations (however tentative) centre on the benefits produced by three factors:

increased spanwise packing; (1.1)

increased VG volume; (1.2)

suitably non-smooth VG shape; (1.3)

and a particular favourable type of VG shape and array is suggested, based on the theory.

2. Assumptions, flow structure, and governing equations

It is assumed that, sufficiently upstream of the VGs, the oncoming turbulent boundary layer is two-dimensional and of the standard two-tiered form, comprising an outer small-velocity-deficit layer of thickness $O(\Delta)$ and an inner stress-dominated sublayer of thickness $O(Re^{-1}\Delta^{-1})$. Here $\Delta = u_\tau^*/u_\infty^*$ is small, of order $(\ln Re)^{-1}$, and we use non-dimensional Cartesian coordinates (x, y, z) (see figure 1), the corresponding velocity components (u, v, w), and the pressure p, non-dimensionalized with respect to l^*, u_∞^*, $\rho^* u_\infty^{*2}$, respectively. The VGs, which for now are taken to be spaced periodically in the spanwise direction z, start at $x = x_0$, say, and are assumed to be slender; specifically, each VG has its characteristic y-dimension (height) of order Δ or less, its characteristic z-dimension (span) and spacing of order Δ, and its x-dimension (length) of order 1 by definition. This is discussed in more detail below. Also, the Reynolds number is taken to be large, as noted earlier. These assumptions seem fairly reasonable for the practical applications in mind.

Our main concern is with the flow in the continuation of the outer deficit layer as it proceeds past and beyond the VGs. Given the VG dimensions above, initially we expect the appropriate scales of the velocity, pressure, and distances to be given by

$$[u, v, w] = [u_e + \Delta u_1, \Delta v_1, \Delta w_1], \quad p = p_e + \Delta^2 p_1, \quad [x, y, z] = [x, \Delta Y, \Delta Z], \quad (2.1\,a\text{–}c)$$

with u_1, v_1, w_1, p_1, x, Y, Z all being typically $O(1)$ and $u_e(x)$ being the non-dimensional external-stream velocity, with corresponding pressure $p_e(x)$ such that $p_e' = -u_e u_e'$. Here the scales (2.1 c) follow directly from the VG geometry and from the thickness of the oncoming outer-deficit layer, along with the expectation that a balance between the Y, Z scales could be significant dynamically. The velocity scales for u_1, v_1 are likewise implied by the oncoming layer properties, since the velocity deficit $u_e - u$ in that layer is $O(\Delta)$, and the w_1-scale then follows from continuity, while the pressure is inferred

from the y- and z-momentum balances. The scales in (2.1 a–c) are adjusted later in this article: see §§3 and 4. The governing equations for the three-dimensional flow induced by the VG, in consequence, are

$$u_e' + \frac{\partial v_1}{\partial Y} + \frac{\partial w_1}{\partial Z} = 0, \quad \left(u_e \frac{\partial}{\partial x} + v_1 \frac{\partial}{\partial Y} + w_1 \frac{\partial}{\partial Z}\right) u_1 + u_1 u_e' = (Tu)_1, \tag{2.2a, b}$$

$$\left(u_e \frac{\partial}{\partial x} + v_1 \frac{\partial}{\partial Y} + w_1 \frac{\partial}{\partial Z}\right) v_1 = -\frac{\partial p_1}{\partial Y} + (Tu)_2, \tag{2.2c}$$

$$\left(u_e \frac{\partial}{\partial x} + v_1 \frac{\partial}{\partial Y} + w_1 \frac{\partial}{\partial Z}\right) w_1 = -\frac{\partial p_1}{\partial Z} + (Tu)_3, \tag{2.2d}$$

for the continuity and the x-, y-, z-momentum balances in turn. The turbulent stress terms $(Tu)_n$, $n = 1, 2, 3$, are detailed below, although they could all be kept quite general as long as they maintain their orders of magnitude: for example, the x-component predominantly has the order of the y-scale times the velocity-gradient-squared, in the current outer layer. The boundary conditions on the nonlinear vortex system (2.2 a–d) are

$$u_1 = u_{2D}(Y), \quad v_1 = v_{2D}(Y), \quad w_1 = 0 \quad \text{at} \quad x = x_0, \tag{2.3a}$$

$$u_1 \to 0, \quad w_1 \to 0 \quad \text{as} \quad Y \to \infty, \tag{2.3b}$$

$$u_1 \sim u_e \ln(Y - F), \quad v_1 \to 0, \quad w_1 \to O(1) \quad \text{as} \quad Y \to F(x, Z). \tag{2.3c}$$

The constraint (2.3 a) joins the flow solution with that of the oncoming two-dimensional boundary layer, which is undisturbed ahead of the start of the VGs at $x = x_0$ because the system (2.2 a–d) is parabolic in x. The condition (2.3 b) holds for the match with the external stream, whereas the condition (2.3 c) corresponds to the match with the inner stress sublayer, close to the VG surface $Y = F(x, Z)$ (with F of order one for now). That sublayer is exponentially thin, in terms of $Y - F$ and Δ. The logarithmic behaviour in the streamwise velocity perturbation in (2.3 c) is necessary to cancel out the external-stream part $u_e(x)$ (see (2.1 a)) in the sublayer, as $Y - F$ decreases to the order $1/\exp(\Delta^{-1})$ approximately, to enable the no-slip condition to be satisfied within the sublayer. Similarly, if a cross-flow component w_e is present in the external stream then w_1 has to produce a $w_e \ln(Y - F)$ response as $Y \to F$. This explains the constraint [a no-logarithm condition] on w_1 in (2.3 c), for the present case with no external cross-flow. Returning to the condition (2.3 a), we observe that the two-dimensional boundary layer upstream, which corresponds to the undisturbed flow with zero $F(x, Z)$, has its solution given by

$$v_1 = -Yu_e'(x), \quad \frac{\partial}{\partial x}(u_e u_1) - Yu_e' \frac{\partial u_1}{\partial Y} = (Tu)_1, \tag{2.4a, b}$$

and $w_1 = 0$, $p_1 = p_1(x, Y)$, consistent with (2.2 a–d). Here in general the profile $u_1 = u_{2D}(Y)$ at $x = x_0$ has to be found from forward marching (2.4 b) from some starting conditions ahead of $x = x_0$, subject to

$$u_1 \to 0 \quad \text{as} \quad Y \to \infty, \quad u_1 \sim u_e \ln Y \quad \text{as} \quad Y \to 0, \tag{2.4c, d}$$

where (2.4 d) in particular is in line with the logarithmic requirement (2.3 c) over the VGs. A special case for this upstream flow is taken later on: see §3.

The Prandtl shift, defined by

$$Y - F = \bar{Y}, \quad v_1 - F_x u_e - F_Z w_1 = V_1, \tag{2.5}$$

is now applied, to simplify the boundary conditions. This changes the three-dimensional governing equations (2.2*a–d*) for the VG flow to the following:

$$u_e' + \frac{\partial V_1}{\partial \bar{Y}} + \frac{\partial w_1}{\partial Z} = 0, \tag{2.6a}$$

$$\left(u_e \frac{\partial}{\partial x} + V_1 \frac{\partial}{\partial \bar{Y}} + w_1 \frac{\partial}{\partial Z}\right) u_1 + u_1 u_e' = \frac{\partial}{\partial \bar{Y}}\left[a_1 \bar{Y}^2 \left(\frac{\partial u_1}{\partial \bar{Y}}\right)^2\right], \tag{2.6b}$$

$$\left(u_e \frac{\partial}{\partial x} + V_1 \frac{\partial}{\partial \bar{Y}} + w_1 \frac{\partial}{\partial Z}\right)(V_1 + F_x u_e + F_Z w_1) = -\frac{\partial p_1}{\partial \bar{Y}} + \frac{\partial}{\partial \bar{Y}}\left[a_1 \bar{Y}^2 \frac{\partial u_1}{\partial \bar{Y}} \frac{\partial V_1}{\partial \bar{Y}}\right], \tag{2.6c}$$

$$\left(u_e \frac{\partial}{\partial x} + V_1 \frac{\partial}{\partial \bar{Y}} + w_1 \frac{\partial}{\partial Z}\right) w_1 = -\frac{\partial p_1}{\partial Z} + F_Z \frac{\partial p_1}{\partial \bar{Y}} + \frac{\partial}{\partial \bar{Y}}\left[a_1 \bar{Y}^2 \frac{\partial u_1}{\partial \bar{Y}} \frac{\partial w_1}{\partial \bar{Y}}\right], \tag{2.6d}$$

where, in addition, the turbulent stress terms are now made specific as shown, as a generalization of the Cebeci–Smith form for the current vortex flows. Other forms (e.g. see §1) could be taken at this stage, but those in (2.6*a–d*) appear not unreasonable, in this first study, given also our eventual concern with low-profile VGs subsequently for which the cross-plane velocities V_1, w_1 are small compared with the streamwise velocity perturbation u_1. Further, the turbulent-stress forms in (2.6*b–d*) hold for an inner range $\bar{Y} < \bar{Y}_1(x, Z)$, and are replaced by displacement-influence terms for the outer range $\bar{Y} > \bar{Y}_1$, e.g. the right-hand side of (2.6*b*) becomes

$$\frac{\partial}{\partial \bar{Y}}\left[a_3 \delta \frac{\partial u_1}{\partial \bar{Y}}\right], \quad \text{where} \quad \delta \equiv -\int_0^\infty u_1 \, \mathrm{d}\bar{Y}, \tag{2.6e}$$

for $\bar{Y} > \bar{Y}_1$, where $\delta(x, Z)$ is the unknown scaled streamwise displacement thickness, and similarly for (2.6*c, d*). The unknown junction $\bar{Y}_1$ is typically of $O(1)$, and the velocity u_1, the shear $\partial u_1/\partial \bar{Y}$ and the stress terms are to be continuous at $\bar{Y} = \bar{Y}_1$, while the constants involved have the values $a_1 = 0.16$, $a_3 = 0.0168$ in this model form. (Later, in §§3–6, it is found that only the inner range as presented in (2.6*b–d*) affects the flow solutions). The boundary conditions now become

$$[u_1, V_1, w_1] = [u_{2D}(\bar{Y}), v_{2D}(\bar{Y}), 0] \quad \text{at} \quad x = x_0, \tag{2.7a}$$

$$u_1 \to 0, \quad w_1 \to 0 \quad \text{as} \quad \bar{Y} \to \infty, \tag{2.7b}$$

$$u_1 \sim u_e \ln \bar{Y}, \quad V_1 \to 0, \quad w_1 \to O(1) \quad \text{as} \quad \bar{Y} \to 0, \tag{2.7c}$$

from (2.3*a–c*), with the assumption that the VG height F starts from zero at $x = x_0$; and the oncoming two-dimensional flow satisfies

$$V_1 = -\bar{Y} u_e', \quad \frac{\partial}{\partial x}(u_e u_1) - \bar{Y} u_e' \frac{\partial u_1}{\partial \bar{Y}} = \frac{\partial}{\partial \bar{Y}}\left[a_1 \bar{Y}^2 \left(\frac{\partial u_1}{\partial \bar{Y}}\right)^2\right] \quad (\text{for} \quad x < x_0), \tag{2.8a, b}$$

with

$$u_1 \to 0 \quad \text{as} \quad \bar{Y} \to \infty, \quad u_1 \sim u_e \ln \bar{Y} \quad \text{as} \quad \bar{Y} \to 0, \tag{2.8c, d}$$

from (2.4*a–d*), with $u_1(x_0, \bar{Y})$ then prescribing $u_{2D}(\bar{Y})$, since $\bar{Y}$ and Y are identical for $x \leqslant x_0$. One main effect, in the transformed version (2.6)–(2.8), is that the influence of the VG shape F makes itself felt in the controlling equations, i.e. in (2.6*c, d*), rather than in the boundary conditions.

The controlling equations, then, are (2.6*a–d*) (for $x > x_0$), with the conditions (2.7*a–c*), (2.8*a–d*), and in general they are fully nonlinear, posing a computational task for forward marching in positive $(x - x_0)$. A computational treatment for the above

system is under development, but more analytical features are investigated in §§3 and 4 below in an attempt to provide extra insight.

Before moving on, we should mention two extra points about the problem (2.6)–(2.8). First, integration of (2.6*b*), (2.6*e*) with respect to $\bar{Y}$ across the layer yields the relation

$$\frac{\partial}{\partial x}[u_e^2\,\delta]-u_e\frac{\partial}{\partial Z}\left[\int_0^\infty u_1\,w_1\,\mathrm{d}\bar{Y}\right]=a_1\,u_e^3, \tag{2.9}$$

involving the displacement function $\delta(x, Z)$. The second term here, a three-dimensional contribution, is due solely to the presence of the VG, and its influence on the displacement function δ is considered further in §§4–6 below. Without the VG, (2.9) would give a direct relation between δ and the free-stream velocity u_e. Secondly the constant a_1 can be factored out of the problem by multiplying $\bar{Y}$, V_1, δ, F, w_1, Z by a_1, in effect, and p_1 by a_1^2, with a_3 then replaced by $a_5 \equiv a_1^{-1}a_3$ ($= 0.105$). So without loss of generality we may henceforth

$$\text{replace}\,(a_1, a_3) \quad \text{by} \quad (1, a_5). \tag{2.10}$$

3. Low-profile VGs

Much progress is possible in the case of 'low-profile' VGs, for which the characteristic height $|F|$ is small, say $F(x, Z) = hf(x, Z)$ where f is typically $O(1)$ but the parameter h is small.

In this case the two-dimensional flow solution is slightly perturbed, in the form

$$[u_1, V_1, w_1] = [u_{10}, V_{10}, 0]+h[u_{11}, V_{11}, w_{11}]+\ldots, \tag{3.1a}$$

with

$$p_1 = p_{10}(x, \bar{Y})+hp_{11}(x, \bar{Y}, Z)+\ldots, \tag{3.1b}$$

where the $O(h)$ perturbations with subscript 11 are dependent on x, $\bar{Y}, Z$ but the leading terms (subscript 10) stand for the two-dimensional solution of (2.8*a–d*), which is independent of Z. Substitution of (3.1*a*, *b*) into the governing equations (2.6*a–d*) reproduces at leading order the equations (2.8*a–d*) for V_{10}, u_{10}, as required, while at the next order the linearized system

$$\frac{\partial V_{11}}{\partial \bar{Y}}+\frac{\partial w_{11}}{\partial Z}=0, \tag{3.2a}$$

$$\left(u_e\frac{\partial}{\partial x}+V_{10}\frac{\partial}{\partial \bar{Y}}\right)u_{11}+V_{11}\frac{\partial u_{10}}{\partial \bar{Y}}+u_{11}u_e'=2\frac{\partial}{\partial \bar{Y}}\left[\bar{Y}^2\frac{\partial u_{10}}{\partial \bar{Y}}\frac{\partial u_{11}}{\partial \bar{Y}}\right], \tag{3.2b}$$

$$\left(u_e\frac{\partial}{\partial x}+V_{10}\frac{\partial}{\partial \bar{Y}}\right)V_{11}+V_{11}\frac{\partial V_{10}}{\partial \bar{Y}}+u_e\frac{\partial}{\partial x}(f_x u_e)=-\frac{\partial p_{11}}{\partial \bar{Y}}+\frac{\partial}{\partial \bar{Y}}\left[\bar{Y}^2\left(\frac{\partial u_{11}}{\partial \bar{Y}}\frac{\partial V_{10}}{\partial \bar{Y}}+\frac{\partial u_{10}}{\partial \bar{Y}}\frac{\partial V_{11}}{\partial \bar{Y}}\right)\right], \tag{3.2c}$$

$$\left(u_e\frac{\partial}{\partial x}+V_{10}\frac{\partial}{\partial \bar{Y}}\right)w_{11}=-\frac{\partial p_{11}}{\partial Z}+f_Z\frac{\partial p_{10}}{\partial \bar{Y}}+\frac{\partial}{\partial \bar{Y}}\left[\bar{Y}^2\frac{\partial u_{10}}{\partial \bar{Y}}\frac{\partial w_{11}}{\partial \bar{Y}}\right], \tag{3.2d}$$

is obtained, for the three-dimensional motion $[u_{11}, V_{11}, w_{11}, p_{11}]$ induced by the low-profile VG. The associated boundary conditions are given below. From (3.2*a*) it follows that a cross-plane streamfunction ψ exists, such that

$$V_{11}=\frac{\partial \psi}{\partial Z}, \quad w_{11}=-\frac{\partial \psi}{\partial \bar{Y}}, \tag{3.3}$$

and so, on elimination of p_{11} between (3.2c, d), ψ satisfies the linear partial differential equation

$$\left(u_e\frac{\partial}{\partial x}+V_{10}\frac{\partial}{\partial \bar{Y}}\right)\nabla^2\psi-u_e'\nabla^2\psi+u_e\frac{\partial}{\partial x}(f_{xZ}u_e)=-f_Z\frac{\partial^2 p_{10}}{\partial \bar{Y}^2}+T. \tag{3.4a}$$

Here ∇^2 denotes the cross-plane Laplacian $(\partial^2/\partial\bar{Y}^2+\partial^2/\partial Z^2)$, $V_{10}\equiv-\bar{Y}u_e'(x)$, and the stress term is

$$T\equiv\frac{\partial}{\partial\bar{Y}}\left[\frac{\partial}{\partial Z}\left\{\frac{\partial u_{10}}{\partial\bar{Y}}\frac{\partial^2\psi}{\partial\bar{Y}\partial Z}+\frac{\partial u_{11}}{\partial\bar{Y}}\frac{\partial V_{10}}{\partial\bar{Y}}\right)\right\}+\frac{\partial}{\partial\bar{Y}}\left\{\bar{Y}^2\frac{\partial u_{10}}{\partial\bar{Y}}\frac{\partial^2\psi}{\partial\bar{Y}^2}\right\}\Bigg], \tag{3.4b}$$

while p_{10}, u_{10} are given by (2.8b–d) in effect. The controlling equation (3.4a) for $\psi(x,\bar{Y},Z)$ is still coupled with (3.2b) for $u_{11}(X,\bar{Y},Z)$, however, via the u_{11} contribution in T in (3.4b) and the $\partial\psi/\partial Z$ contribution in V_{11} in (3.2b). Moreover, the switch corresponding to (2.6e) still holds for $\bar{Y}$ exceeding $\bar{Y}_1$.

Suppose next that the development length of the oncoming two-dimensional boundary layer is relatively long compared with the VG length. This means that the range of interest, initially at least, has

$$x=x_0+X,\quad\text{with}\quad x_0\,\text{large},\quad X\sim 1. \tag{3.5a}$$

Then the typical $\bar{Y}$-scale of the VG flow remains $O(1)$ but the thickness of the oncoming boundary layer is much larger, typically $O(x_0)$ if the imposed pressure gradient upstream of the VG is not too extreme, and the junction position $\bar{Y}_1$ is of the same large scale. Hence the junction $\bar{Y}_1$ lies outside the sublayer $\bar{Y}\sim 1$ of interest and has negligible influence on the flow there. Hence also the oncoming boundary layer effectively has

$$u_{10}(\bar{Y})=u_e\ln\bar{Y}+c_1,\quad V_{10}=O(x_0^{-1}),\quad p_{10}=O(x_0^{-1}), \tag{3.5b}$$

as far as the VG-induced flow is concerned, i.e. for X, $\bar{Y}\sim 1$, where $u_e=u_e(x_0)+O(x_0^{-1})$ varies on the longer scale and so may be treated as constant to leading order, as may c_1. The cross-plane part (3.4a, b) is then de-coupled from the streamwise part (3.2b), and we are left with solving

$$u_e\frac{\partial}{\partial X}(\nabla^2\psi)+u_e^2 f_{XXZ}=u_e\frac{\partial}{\partial\bar{Y}}\left[\bar{Y}\frac{\partial^3\psi}{\partial\bar{Y}\partial Z^2}+\frac{\partial}{\partial\bar{Y}}\left(\bar{Y}\frac{\partial^2\psi}{\partial\bar{Y}^2}\right)\right] \tag{3.6a}$$

for $\psi(X,\bar{Y},Z)$ in $X\geqslant 0$, subject to the boundary conditions

$$\psi=0\quad\text{at}\quad X=0, \tag{3.6b}$$

$$\frac{\partial\psi}{\partial Z}\to-u_e f_X\quad\text{as}\quad\bar{Y}\to\infty, \tag{3.6c}$$

$$\psi=O(\bar{Y})\quad\text{as}\quad\bar{Y}\to O+, \tag{3.6d}$$

from (2.7a–c), respectively. Here again, the assumption involved, namely that *the low-profile VG lies mostly within the logarithmic layer of the oncoming boundary layer*, as is evident from (3.5b), seems sensible in terms of the practical application.

If now the VG distribution is taken to be periodic in Z, and even about $Z=0$, with its shape in the Fourier-series form

$$f(X,Z)=\sum_{n=0}^{\infty}f_n(X)\cos(n\beta Z), \tag{3.7}$$

then the solution can be expressed as

$$\psi=\sum_{n=0}^{\infty}\psi_n(X,\bar{Y})\sin(n\beta Z). \tag{3.8}$$

So from (3.6*a*) the governing equation for the typical Fourier component $\psi_n (= \Psi$ say) here becomes

$$\frac{\partial}{\partial X}\left(\frac{\partial^2 \Psi}{\partial \bar{Y}^2} - b^2 \Psi\right) - b u_e \frac{\mathrm{d}^2 f_n}{\mathrm{d}X^2} = \frac{\partial}{\partial \bar{Y}}\left[-b^2 \bar{Y}\frac{\partial \Psi}{\partial \bar{Y}} + \bar{Y}\frac{\partial^3 \Psi}{\partial \bar{Y}^3} + \frac{\partial^2 \Psi}{\partial \bar{Y}^2}\right], \tag{3.9a}$$

with $b \equiv n\beta$, and the boundary conditions become

$$\Psi = 0 \quad \text{at} \quad X = 0, \tag{3.9b}$$

$$b\Psi \to -u_e \frac{\mathrm{d}f_n}{\mathrm{d}X} \quad \text{as} \quad \bar{Y} \to \infty, \tag{3.9c}$$

$$\Psi = O(\bar{Y}) \quad \text{as} \quad \bar{Y} \to O+, \tag{3.9d}$$

from (3.6*c–d*).

Solutions for (3.9*a–d*) are addressed in the following section. In passing, however, we should mention a number of other aspects here. First, the Fourier decomposition as in (3.7), (3.8) could be applied earlier, to (3.2*a–d*) or (3.4*a*, *b*) as well as to (3.6*a–d*). Secondly, the present controlling equations (3.9*a–d*) preserve the inertial-stress balance, in what is effectively the logarithmic region of the boundary layer. The same is true for the earlier equations (3.2), (3.4) and (3.6) and their nonlinear counterpart in §2. Thirdly, the mean-flow component ($n = 0$) in the decomposition (3.8) is identically zero in effect. More precisely, we have V_{11}, w_{11} both being zero and $\partial p_{11}/\partial \bar{Y} = -u_e^2 f_0'''(X)$ for the $n = 0$ component when (3.5*a*, *b*) hold. Fourthly, if u_e is taken to be uniform throughout, i.e. for all x, as distinct from the local property in (3.5*b*), then $V_{10} = \partial p_{10}/\partial \bar{Y} \equiv 0$ throughout and so (3.4*a*, *b*) again decouple from (3.2*b*), leaving the controlling equation as

$$u_e \frac{\partial}{\partial x}(\nabla^2 \psi) + u_e^2 f_{xxz} = \frac{\partial}{\partial \bar{Y}}\left[\bar{Y}^2 \frac{\partial u_{10}}{\partial \bar{Y}}\frac{\partial^3 \psi}{\partial \bar{Y}\partial Z^2} + \frac{\partial}{\partial \bar{Y}}\left\{\bar{Y}^2 \frac{\partial u_{10}}{\partial \bar{Y}}\frac{\partial^2 \psi}{\partial \bar{Y}^2}\right\}\right], \tag{3.10a}$$

subject to (3.6*b–d*) again, with x replacing X and $x = x_0$ replacing $X = 0$. In this case the basic two-dimensional contribution $u_{10}(x, \bar{Y})$ is determined by solving

$$u_e \frac{\partial u_{10}}{\partial x} = \frac{\partial}{\partial \bar{Y}}\left[\bar{Y}^2 \left(\frac{\partial u_{10}}{\partial \bar{Y}}\right)^2\right] \tag{3.10b}$$

(for $\bar{Y} < \bar{Y}_1$, and similarly, for $\bar{Y} > \bar{Y}_1$), which admits a similarity solution (see Neish & Smith 1988). Then the formulation in (3.9*a–d*) may be confirmed as a limiting case from (3.10*a*, *b*). Other simple $u_e(x)$ distributions upstream of the VG, e.g. for an adverse pressure gradient, likewise yield a check on the formulation (3.9*a–d*). Fifthly, the possible use of a_5 as a small parameter (as in Neish & Smith 1988) is noted. This acts to simplify the effects of the junction $\bar{Y}_1$ in the formulation prior to (3.5*a*), and it again confirms (3.9) in the appropriate limit. Sixthly, if the low-VG profile is sufficiently short then the flow response can become nonlinear again. The latter occurs if the X and Z variations are reduced to $O(h)$, in fact, from inspection, since then the appropriate scalings with h are found to re-instate the nonlinear balance in (2.6*a–d*). Our main concern next, however, is with the solution properties of (3.9*a–d*).

4. Analytical and computational properties, for single-mode VGs

In this section and the next we consider individual Fourier components, or single-mode VGs, as forerunners for the practical shapes addressed later in §6.

The computations and the analysis below were performed almost simultaneously. We consider the computations first.

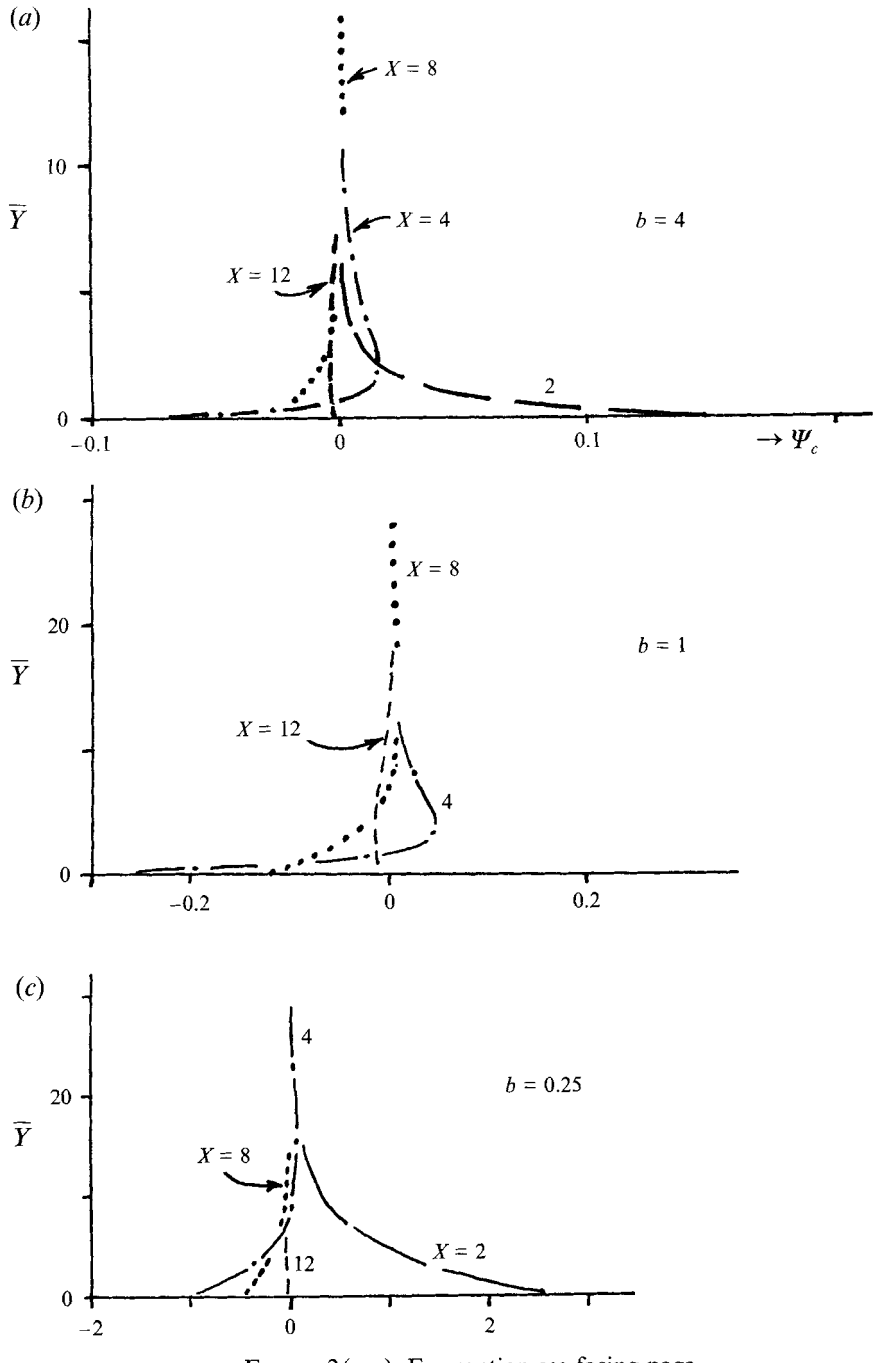

FIGURE 2(*a–c*). For caption see facing page.

Computational solutions of (3.9*a–d*) were obtained by use of a forward-marching scheme analogous to the Crank–Nicolson approach. The new variable $q(X, \bar{Y})$ was introduced, defined by

$$q = \bar{Y} \frac{\partial^2 \Psi_c}{\partial \bar{Y}^2}, \tag{4.1a}$$

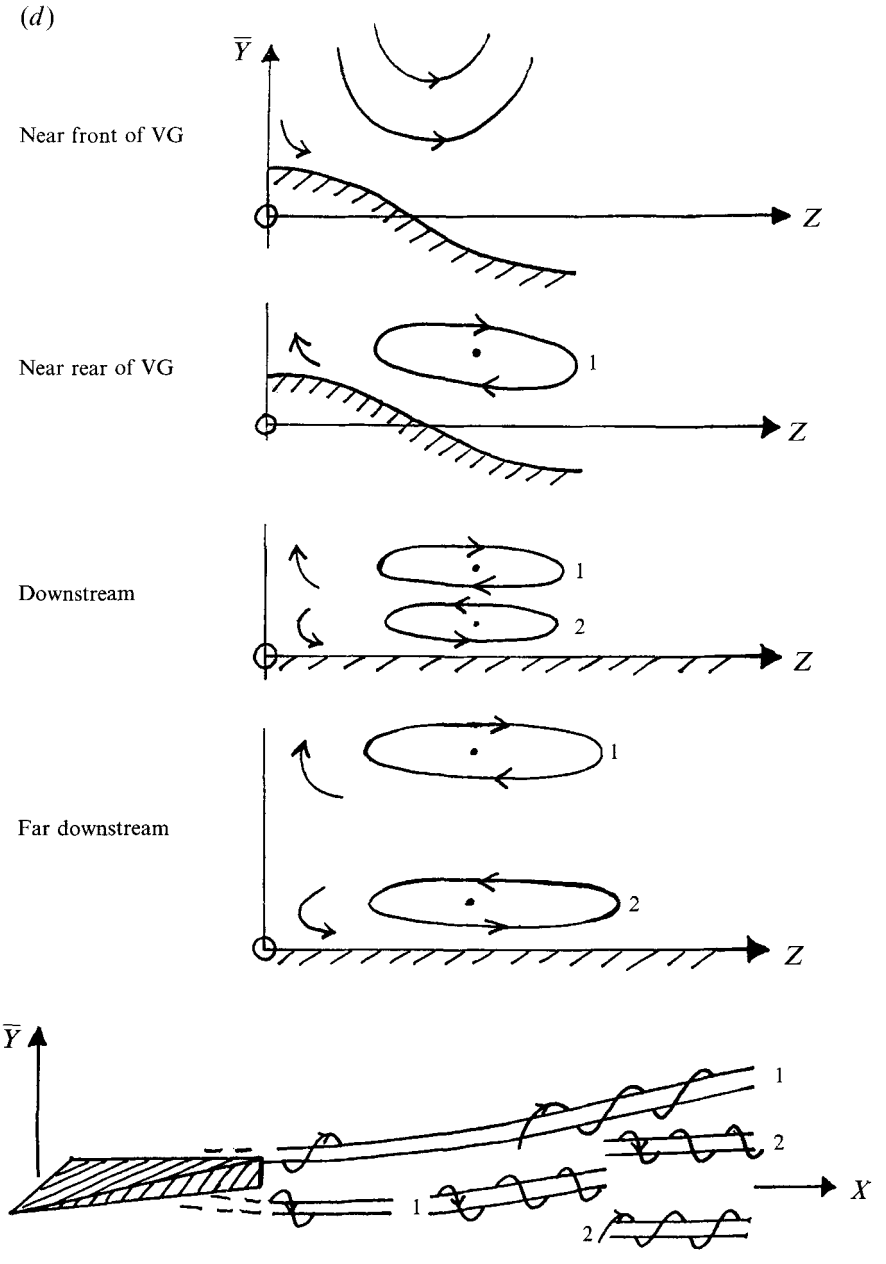

FIGURE 2. Results for §4. (*a*)–(*c*), computed profiles of cross-plane streamfunction. (*d*), the development of vortex flow downstream (schematic, see also appendix A).

so that (3.9*a*) could be re-written as

$$\frac{\partial}{\partial X}\left(\frac{q}{\bar{Y}}-b^2\Psi_c\right)=-b^2\left(\frac{\partial\Psi_c}{\partial\bar{Y}}+q\right)+\frac{\partial^2 q}{\partial\bar{Y}^2} \tag{4.1b}$$

where $\Psi_c \equiv \Psi+b^{-1}u_e\,\mathrm{d}f_n/\mathrm{d}X$ is an effective deficit streamfunction. The two equations (4.1*a*, *b*), involving only second derivatives in $\bar{Y}$, were then discretized with three-point

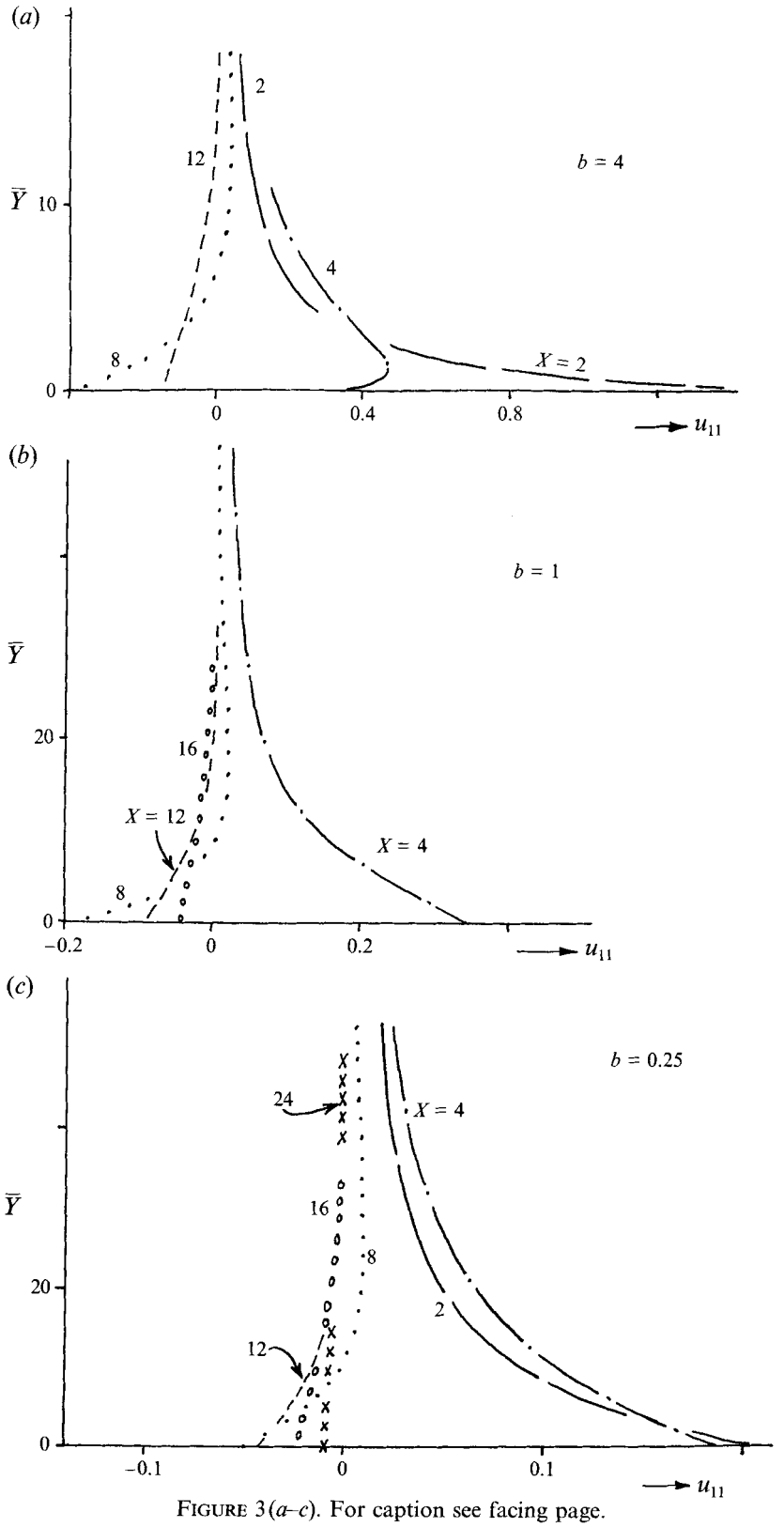

FIGURE 3(*a–c*). For caption see facing page.

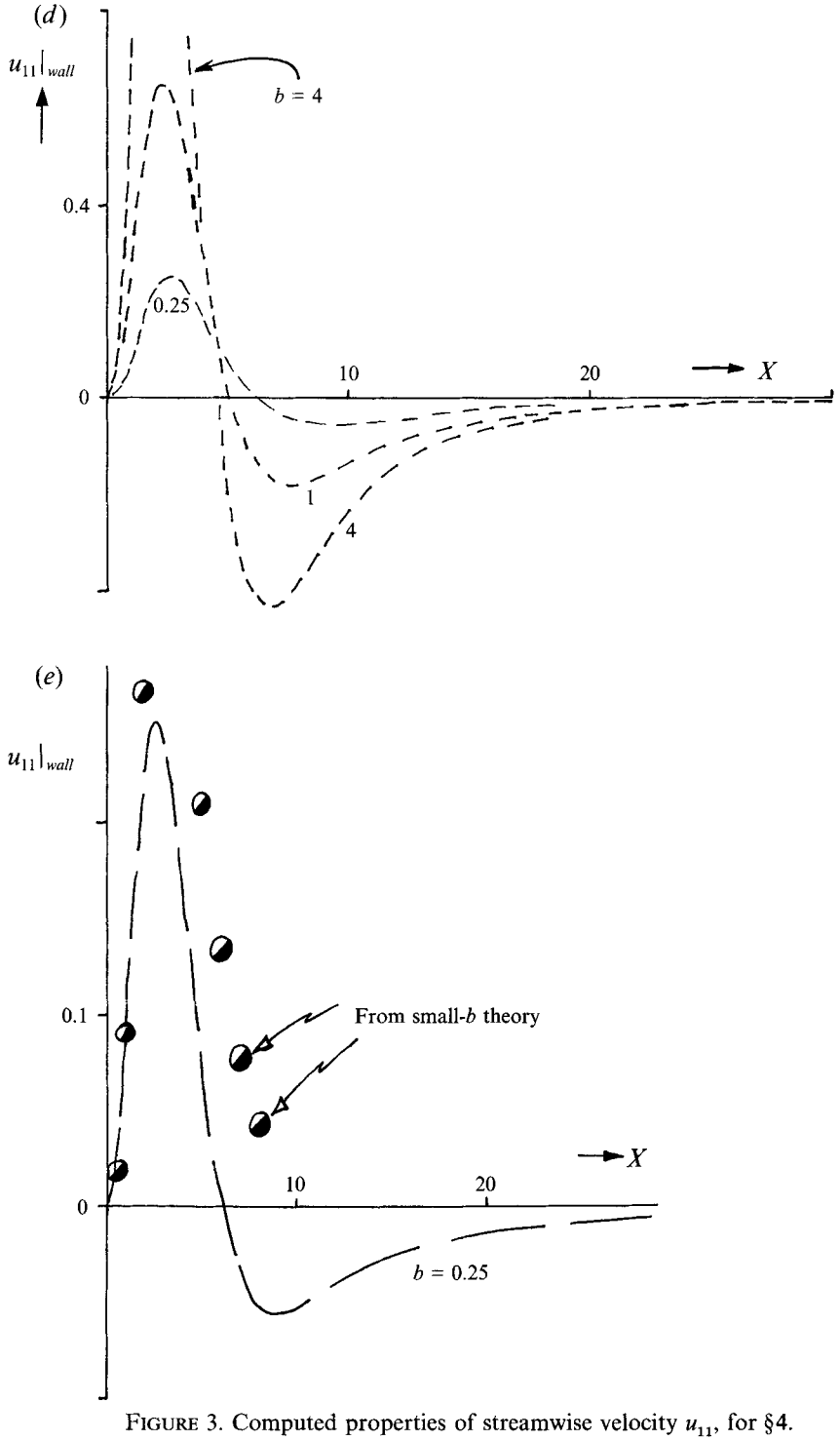

FIGURE 3. Computed properties of streamwise velocity u_{11}, for §4.

formulae in $\bar{Y}$ (step $\Delta\bar{Y}$) and two-point in X (step ΔX) followed by inversion of a tri-diagonal matrix. The accuracy achieved is similar to or greater than that described later in §6. The treatment of the inner boundary condition (3.9d) involved setting Ψ_c, q equal to $b^{-1}u_e\,\mathrm{d}f_n/\mathrm{d}X$, zero, respectively, at $\bar{Y}=0$. Solutions for u_{11} were obtained by a similar X-marching procedure applied to (3.2b), and certain integral properties were also computed from the solutions at each station. Care also had to be taken in treating the slow $\bar{Y}$-decay of part of the solutions. At the outer edge $\bar{Y}_\infty$, u_{11} was set equal to u_{11} at the previous station plus $\bar{Y}_\infty^{-1}\Delta X\,\mathrm{d}f_n/\mathrm{d}X$, in line with (3.2$b$), (3.3), (3.6$c$), whereas Ψ_c, q there were set to zero because of (3.9c). This proved to be a sufficiently accurate representation as subsequent tests show.

The main computational results obtained are presented in figures 2–4.. These include the profiles of the cross-plane streamfunction Ψ and the streamwise velocity component u_{11}, at various X stations, along with the X-variation of the integral properties

$$r_1 \equiv \int_0^\infty \left[\Psi + b^{-1}u_e\frac{\mathrm{d}f_n}{\mathrm{d}X}\right]\mathrm{d}\bar{Y}, \quad r_2 \equiv \int_0^\infty \frac{\partial\Psi}{\partial\bar{Y}}\ln\bar{Y}\,\mathrm{d}\bar{Y}, \tag{4.2a, b}$$

gauging the deficit and the complete displacement effects respectively (see also (4.2e,f) below), and the (negative) component

$$r_3 \equiv \frac{\partial\Psi}{\partial\bar{Y}}(X,O) \tag{4.2c}$$

of the spanwise slip velocity w_{11} induced at $\bar{Y}=O+$. The particular shape chosen (for the nth component) was

$$u_e f_n(X) = X^3\exp(-X), \tag{4.2d}$$

to illustrate matters, and solutions for various values of b were investigated. Another integral property of concern is

$$r_4 \equiv \int_0^X r_2(X)\,\mathrm{d}X, \tag{4.2e}$$

since the influence ($h\delta_1$) of the low-profile VG on the displacement function δ ($=\delta_0+h\delta_1$) is given by

$$\delta_1 = c_1 f - \sum_{n=0}^{\infty} n\beta r_4(X)\cos(n\beta Z), \tag{4.2f}$$

from (2.9). Here $\delta_0 \equiv O(x_0)+O(X)$. The computed variation of r_4 with X is also presented in the figures.

The solutions of (3.9a–d) can also be obtained analytically, however, in principle. The Laplace transform in X, defined by

$$\Psi^L \equiv \int_0^\infty \left[\Psi(X,\bar{Y}) + b^{-1}u_e\frac{\mathrm{d}f_n}{\mathrm{d}X}\right]\mathrm{e}^{-sX}\,\mathrm{d}X \tag{4.3}$$

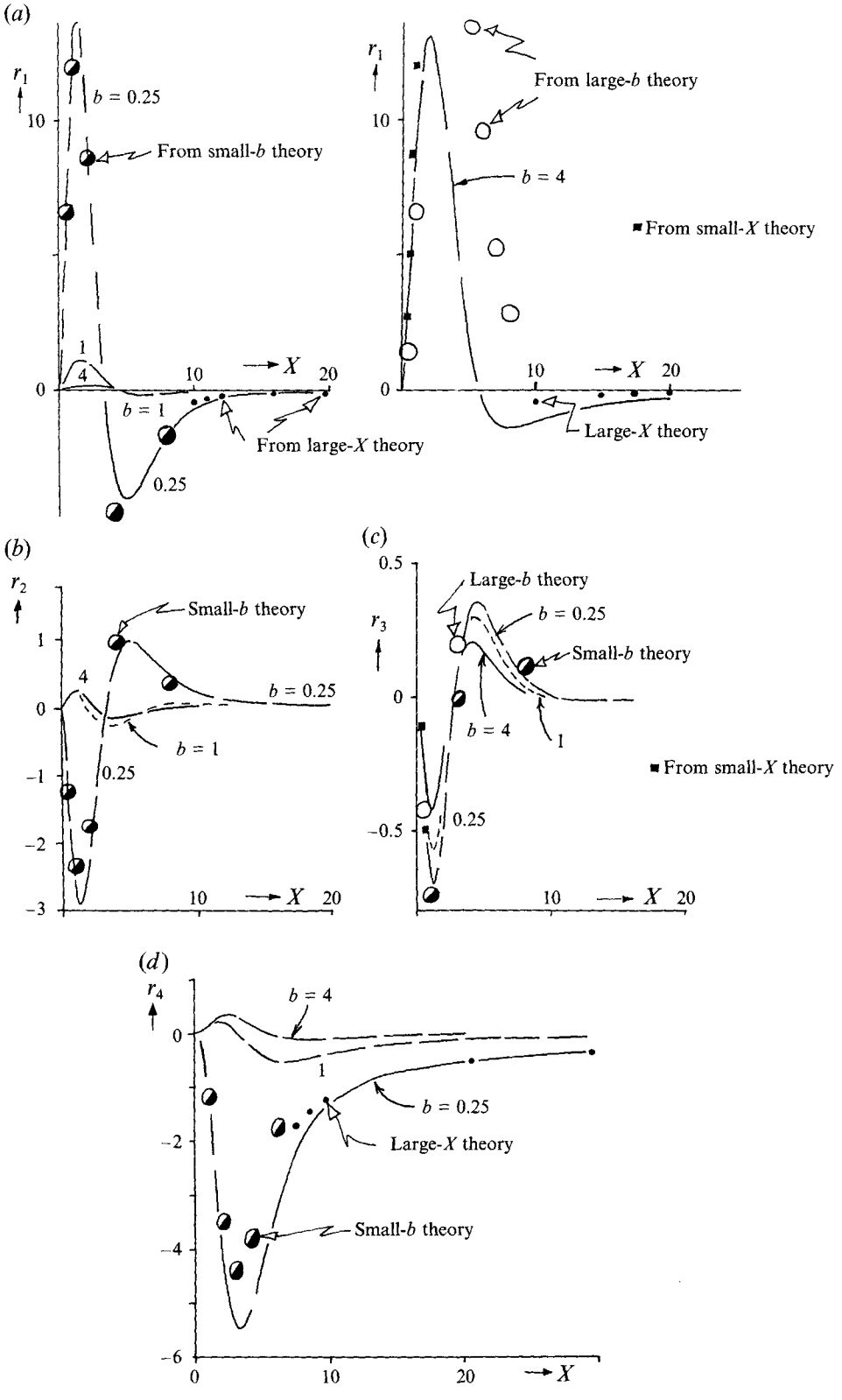

FIGURE 4. Computed results for r_1, r_2, r_3, r_4 versus X, for §4.

(where the added term is included for convenience), converts (3.9a) to the fourth-order ordinary differential equation

$$s\left(\frac{\partial^2 \Psi^L}{\partial \bar{Y}^2} - b^2 \Psi^L\right) = \frac{\partial}{\partial \bar{Y}}\left(-b^2 \bar{Y} \frac{\partial \Psi^L}{\partial \bar{Y}} + \bar{Y} \frac{\partial^3 \Psi^L}{\partial \bar{Y}^3} + \frac{\partial^2 \Psi^L}{\partial \bar{Y}^2}\right) \tag{4.4a}$$

for $\Psi^L(s, \bar{Y})$, on use of the starting condition (3.9b). The constraints (3.9c, d) become

$$\Psi^L \to 0 \quad \text{as} \quad \bar{Y} \to \infty, \tag{4.4b}$$

$$\Psi^L \sim b^{-1} u_e s f_n^L(s) + O(\bar{Y}) \quad \text{as} \quad \bar{Y} \to O+, \tag{4.4c}$$

where L denotes transformed quantities. Each of the (4.4b, c) really serves as two boundary conditions, from analysis of the behaviour at large and small $\bar{Y}$. Thus from (4.4a, b) the solution may be shown to have the integral form

$$\Psi^L = e_1(s) \int_b^\infty \frac{\exp(-r\bar{Y} - r^{-1}s)\,\mathrm{d}r}{r(r^2 - b^2)^{\frac{1}{2}}} + e_2(s) \int_0^b \frac{\exp(-r\bar{Y} - r^{-1}s)\,\mathrm{d}r}{r(b^2 - r^2)^{\frac{1}{2}}} \tag{4.5a}$$

with the two functions e_1, e_2 to be determined. However, the $\bar{Y}$-derivative of the first integral here is logarithmic as $\bar{Y} \to 0$, whereas that of the second integral is finite. Hence, (4.4c) yields the two results

required, where

$$e_1 = 0, \quad e_2 = I^{-1} b^{-1} u_e s f_n^L \tag{4.5b}$$

$$I = \int_0^b \frac{\mathrm{e}^{-s/r}\,\mathrm{d}r}{r(b^2 - r^2)^{\frac{1}{2}}} = b^{-1} K_0\left(\frac{s}{b}\right) \tag{4.5c}$$

and K_0 is a modified Bessel function in the standard notation. In principle, (4.5a, b) may then be used to give the solution $\Psi(X, \bar{Y})$ as an inverse transform or convolution integral. The advantage of the analytical method is that it applies for any VG shape f_n, of course. In practice, the computational method (see earlier) is probably easier to apply for particular shapes, but the exact analytical expression in (4.5a, b) provides a very helpful check on the accuracy of the computations, as well as yielding some general results. In particular, (4.5a, b) lead to the far-downstream predictions, for the quantities defined in (4.2a–c),

$$r_1 \sim -b^{-1} u_e a X^{-1} (\ln X)^{-2}, \quad r_2 \sim \tfrac{1}{2} b^{-1} u_e a X^{-2}, \quad r_3 \sim -\tfrac{1}{2} u_e a \pi X^{-2} (\ln X)^{-2}, \tag{4.6a–c}$$

after some working, details of which are available from the author. Here the far-downstream response is controlled by the net VG cross-plane area

$$a \equiv \int_0^\infty f_n(X)\,\mathrm{d}X, \tag{4.7}$$

we note, whereas the response at most X values of $O(1)$ is shape-dependent, i.e. depends specifically on the particular VG shape, rather than on a net quantity such as (4.7). Asymptotes at small X are also obtainable, nevertheless, from (4.5a, b); for example we have

$$r_1 \sim b^{-2} u_e f_n'(X), \quad r_3 \sim -u_e f_n'(X), \quad \text{at small} \quad X, \tag{4.8a, b}$$

and these are shown in comparisons in the figures. The predictions (4.6a–c), (4.8a, b) agree well with the computations, as is demonstrated in the figures.

The far-downstream behaviour is also of importance for other reasons, as we shall see later, and it is worth addressing in more detail. The major feature, for large positive X, is that the current (logarithmic) layer starts to split into two zones then, one staying close to the surface, with $\bar{Y}$ remaining $O(1)$, and the other spreading out quite rapidly, with its typical $\bar{Y}$ values increasing in proportion to X. The details are presented in Appendix A.

Other features can also be examined, e.g. those for small X. Also, the response in the nonlinear regime is expected to be similar far downstream to that in (4.6) as the VG effect peters out.

The changes in the flow response as X increases are very interesting, as indeed comparisons between the positive and negative behaviours in (4.6*a*, *c*), (4.9*a*, *b*) would suggest. The maximum responses tend to occur relatively near the VG, followed by more gradual trends towards the asymptotes of (4.6*a–c*). The results for increasing X appear to indicate a down-wash (in $\bar{Y}$), then up-wash, then both, accompanied by spanwise out-wash (in Z) near the surface, then in-wash, then out-wash, as shown in figure 2(*d*). The vortex centres are also of interest here; we note that a double system of longitudinal streamwise vortices appears sufficiently far downstream, see figure 2(*d*) again and also Appendix A. One might like to believe the results in the figures above are typical of those for any reasonable VG shape, of course, and indeed comparisons may be drawn with the work in §6 below on realistic VG shapes.

5. Influence of the spanwise variation, for single-mode VGs

The findings in the preceding section on single-mode VGs indicate three main factors with regard to the spanwise VG distribution, and these are considered in (i)–(iii) below, before we turn to realistic VG shapes in the next section.

(i) *Slow spanwise variation*

This corresponds mathematically to small values of b and physically to cases of comparatively gentle variation in both the VG shape and the spacing in the spanwise direction. For small b (but still $b \gg \Delta$ probably, to preserve the validity of (3.9)) the flow solution of (3.9*a–d*) develops on two different streamwise lengthscales, namely $X \sim 1$ and $X \sim b^{-1}$. The first stage here has

$$\Psi = b^{-1}\Psi_0 + \Psi_1 + b\Psi_2 + \ldots \quad (X = O(1)), \tag{5.1}$$

with $\bar{Y} = b^{-1}\bar{\bar{Y}}$ typically being large. Hence from (3.9*a*) the successive governing equations for the contributions in (5.1) are

$$\frac{\partial}{\partial X}\left(\frac{\partial^2 \Psi_0}{\partial \bar{\bar{Y}}^2} - \Psi_0\right) - u_e \frac{\mathrm{d}^2 f_n}{\mathrm{d}X^2} = 0, \tag{5.2a}$$

$$\frac{\partial}{\partial X}\left(\frac{\partial^2 \Psi_1}{\partial \bar{\bar{Y}}^2} - \Psi_1\right) = \frac{\partial}{\partial \bar{\bar{Y}}}\left[-\bar{\bar{Y}}\frac{\partial \Psi_0}{\partial \bar{\bar{Y}}} + \bar{\bar{Y}}\frac{\partial^3 \Psi_0}{\partial \bar{\bar{Y}}^3} + \frac{\partial^2 \Psi_0}{\partial \bar{\bar{Y}}^2}\right], \tag{5.2b}$$

$$\frac{\partial}{\partial X}\left(\frac{\partial^2 \Psi_2}{\partial \bar{\bar{Y}}^2} - \Psi_2\right) = \frac{\partial}{\partial \bar{\bar{Y}}}\left[-\bar{\bar{Y}}\frac{\partial \Psi_1}{\partial \bar{\bar{Y}}} + \bar{\bar{Y}}\frac{\partial^3 \Psi_1}{\partial \bar{\bar{Y}}^3} + \frac{\partial^2 \Psi_1}{\partial \bar{\bar{Y}}^2}\right], \tag{5.2c}$$

and so on. Given the zero starting conditions from (3.9*b*), the solutions of (5.2*a–c*) and the appropriate boundary conditions may be obtained successively as:

$$\Psi_0 = -u_e f_n'(X) + A_0 \exp(-\bar{Y}), \quad A_0 \equiv u_e f_n', \tag{5.3a}$$

$$\Psi_1 = B_1 \bar{Y} \exp(-\bar{Y}), \quad B_1 \equiv \tfrac{1}{2} u_e f_n, \tag{5.3b}$$

$$\Psi_2 = (B_2 \bar{Y} + C_2 \bar{Y}^2) \exp(-\bar{Y}), \quad B_2 = -\tfrac{7}{3} C_2 \equiv -\tfrac{7}{4} \int_0^X B_1 \, dX. \tag{5.3c}$$

From these results, the behaviours of the particular properties in (4.2*a–c*) are then found to be

$$r_1 = b^{-2}[u_e f_n'] + b^{-1}[\tfrac{1}{2} u_e f_n] + [B_2 + 2C_2] + O(b), \tag{5.4a}$$

$$r_2 = b^{-1}[\ln b + \gamma] u_e f_n' - [\tfrac{1}{2} u_e f_n] + b[-\tfrac{3}{2} C_2 \ln b - B_2 - C_2] + O(b^2), \tag{5.4b}$$

$$r_3 = [-u_e f_n'] + b[\tfrac{1}{2} u_e f_n] + b^2 [B_2] + O(b^3), \tag{5.4c}$$

where $\gamma = 0.5772\ldots$ is Euler's constant. Clearly, the motion is inertia-dominated at leading order, yielding the inertial result (5.3*a*) and the leading terms in (5.4*a–c*). All these leading first-order effects continue for those X stations where the VG is present but then stop where the VG stops, however, since they depend on the slope f_n'. The same applies to the second-order effects, which depend on the shape f_n (see (5.3*b*) and the second terms in (5.4*a–c*)). The persistent effects downstream of the VG appear mainly in the third-order terms, since they involve there the net quantity a (defined in (4.7)). In consequence,

$$\Psi \to b(-7\bar{Y} + 3\bar{Y}^2) \exp(-\bar{Y}) \frac{u_e}{8} a, \tag{5.5a}$$

$$r_1 \to -\frac{u_e}{8} a, \tag{5.5b}$$

$$r_2 \to b[-9 \ln b + 8] \frac{u_e}{16} a, \tag{5.5c}$$

$$r_3 \to b^2 (-\tfrac{7}{8}) u_e a, \tag{5.5d}$$

behind the VG. It is of interest that the responses (5.5*a–d*) (to within $O(b)$) therefore persist for a considerable distance downstream. From the above, the behaviour of r_4, u_{11} can also be evaluated for small b, giving for instance

$$u_{11W} = b[u_e f_n] + b^2 \left[-\tfrac{3}{2} u_e \int_0^X f_n(X) \, dX \right] + O(b^3) \tag{5.5e}$$

for the nth component, at X values of $O(1)$, but

$$r_4 \to [-\tfrac{1}{2} u_e a], \tag{5.5f}$$

$$u_{11} \to b^2 [-\exp(-\bar{Y}) + 4\bar{Y}^{-2}\{1 - (1 + Y + Y^2) \exp(-\bar{Y})\}] \frac{u_e a}{2}, \tag{5.5g}$$

downstream of the VG, to leading order, on analysis of (3.2*b*). We note the increase in the order of magnitude for r_4 in (5.5*f*) compared with the order of magnitude of r_2

in (5.5*c*). Comparisons with the earlier computations support the predictions above for small values of b, as the figures show.

The second stage occurs far downstream where $X = b^{-1}\bar{X}$ say, with $\bar{X}$ of $O(1)$. There the full governing equation (3.9*a*) is retrieved, with $\bar{X}$ replacing X and $\bar{Y}$ replacing $\bar{Y}$, and f_n is effectively zero now in (3.9*c*). Also, Ψ is small, of order b. The starting condition is unusual, however, in that $b^{-1}\Psi$ is given by (5.5*a*) at $\bar{X} = O+$. With account taken for that, the solution may be obtained by the transform method as in §4, leading eventually to the results (4.6*a–c*), holding far downstream at large $\bar{X}$.

The main attribute of the small-b range, then, is the splitting of the streamwise scale into two stages, one being inertia-dominated in a sense, and the other being elongated to restore the inertia–stress balance. Thus the attainment of the far-downstream behaviour (4.6*a–c*) is delayed in this case.

(ii) *Rapid spanwise variation*

Here b is large, corresponding to relatively fast spanwise variation in the VG slope and/or spacing. For large b, there are again two stages in the streamwise dependence. The first stage has X scaled small of order b^{-1}, say $X = b^{-1}\bar{X}$, with $\bar{Y} = b^{-1}\bar{Y}$ of the same order. So then the full system (3.9*a–d*) still holds, retaining the inertia–stress balance, but with the simplifying feature that the effective VG shape f_n is replaced by its starting form. In the case of (4.2*d*), for example, this means that X^3 replaces f_n. The solution then has the form in (4.3)–(4.5*c*), leading in particular to the downstream asymptotes

$$r_1 \sim b^{-4} u_e \bar{X}^3 (\ln \bar{X})^{-1}, \quad r_2 \sim -\tfrac{3}{2} b^{-3} u_e \bar{X}^2 \ln \bar{X} \quad r_3 \sim -\tfrac{3}{2} b^{-2} u_e \pi \bar{X}^2 (\ln \bar{X})^{-3}, \tag{5.6a–c}$$

at large $\bar{X}$, for the case of the VG shape (4.2*d*).

The second stage, further downstream where X becomes $O(1)$ and the entire VG shape influences matters, is therefore two-layered in structure. The outer layer has $\bar{Y}$ of $O(1)$ and the expansion

$$\Psi + b^{-1} u_e f_n'(X) = b^{-1}[(\ln b)^{-1}\psi_0 + O(\ln b)^{-2}] \tag{5.7}$$

holds. Here the $\ln b$ factors have to be included because of the logarithmic growth found below. The governing equation becomes

$$\frac{\partial \psi_0}{\partial X} = \frac{\partial}{\partial \bar{Y}}\left(\bar{Y}\frac{\partial \psi_0}{\partial \bar{Y}}\right), \tag{5.8a}$$

preserving an inertia-stress balance, while the appropriate boundary conditions are now

$$\psi_0 \to 0 \quad \text{as} \quad X \to 0, \quad \psi_0 \to 0 \quad \text{as} \quad \bar{Y} \to \infty, \quad \psi_0 \sim -u_e f_n' \ln \bar{Y} \quad \text{as} \quad \bar{Y} \to 0. \tag{5.8b–d}$$

The logarithmic condition (5.8*d*) in particular needs a comment. It arises because in the inner layer, where $\bar{Y}$ is small and $O(b^{-1})$, the solution takes the form

$$\Psi = b^{-1}[(\ln b)^{-1}\tilde{\psi}_1 + O(\ln b)^{-2}], \tag{5.9}$$

with $\bar{Y} = b^{-1}\tilde{Y}$. Hence the matching with (5.7) is achieved satisfactorily provided that

$$\tilde{\psi}_1 \sim -u_e f_n' \ln \tilde{Y} + O(1) \quad \text{as} \quad \tilde{Y} \to \infty. \tag{5.10a}$$

Further, $\tilde{\psi}_1$ satisfies the stress-dominated controlling equation

$$0 = \frac{\partial}{\partial \tilde{Y}}\left[-\tilde{Y}\frac{\partial \tilde{\psi}_1}{\partial \tilde{Y}} + \tilde{Y}\frac{\partial^3 \tilde{\psi}_1}{\partial \tilde{Y}^3} + \frac{\partial^2 \tilde{\psi}_1}{\partial \tilde{Y}^2}\right] \tag{5.10b}$$

and the boundary conditions

$$\tilde{\psi}_1 = 0 \quad \text{at} \quad X = 0, \quad \tilde{\psi}_1 = 0(\tilde{Y}) \quad \text{as} \quad \tilde{Y} \to 0, \tag{5.10c,d}$$

in addition to (5.10*a*).

The solution of (5.8*a*–*d*) for the outer layer is found to be, in transform terms,

$$\psi_0^L = -u_e s f_n^L(s) \int_0^\infty r^{-1} \exp(-r\bar{Y} - r^{-1}s)\, \mathrm{d}r. \tag{5.11a}$$

In the inner layer, on the other hand, we find the solution

$$\tilde{\psi}_1 = u_e f_n' \int_0^{\tilde{Y}} \left[I_0(\tilde{Y}) \int_\infty^{\tilde{Y}} K_0(q)\, \mathrm{d}q - K_0(\tilde{Y}) \int_0^{\tilde{Y}} I_0(q)\, \mathrm{d}q \right] \mathrm{d}\tilde{Y} \tag{5.11b}$$

from (5.10*a*–*d*), where I_0 is a standard modified Bessel function.

The overall VG-flow properties r_1, r_2, r_3, r_4, and the streamwise velocity perturbation u_{11}, then depend on (5.11*a*) and/or (5.11*b*), in this b-large extreme. Thus r_1 is dominated by the outer-layer contribution, giving

$$r_1(X) = \frac{u_e f_n(X)}{b \ln b} + \ldots \tag{5.12a}$$

from (5.11*a*) (or from directly integrating (5.8*a*) with respect to $\bar{Y}$). A formula for $r_2(x)$ can also be worked out, using a combination of (5.11*a*, *b*). The result for r_3 is

$$r_3(X) = -\tfrac{1}{2}\pi u_e f_n' (\ln b)^{-1} + \ldots \tag{5.12b}$$

from the inner-layer behaviour, and r_4 follows similarly from (4.2*e*), given r_2 as mentioned above. The results here match with (5.6*a*–*c*) at small X. Finally, the response of the streamwise velocity perturbation may be derived by combining (3.2*b*) with (5.11*a*, *b*) in the inner and outer layers, indicating that the nth component of u_{11} is of the order unity to within a power of $\ln b$.

Comparisons (see figures) with the computations at large values of b are fairly affirmative for the large-b description above. The major flow features in this case are: the two streamwise stages produced, one short, the other of $O(1)$; the two-layered structure during the latter stage; and the logarithmic effects provoked between the two layers, with one layer being stress-dominated and the other being inertia-stress controlled.

(iii) *The isolated VG*

This corresponds to the spanwise spacing becoming infinite, in essence, but with the VG shape finite, thus combining some of the effects in both (i), (ii) above. The isolated VG here satisfies (3.6*a*–*d*) but the periodic decomposition (3.7) ff no longer holds, since

now the VGs effects on the flow must instead decay as $Z \to \pm\infty$ (compare §6 below). Hence a Fourier transform in Z is appropriate, in general, of the form

$$\hat{\psi}(X, \bar{Y}, \omega) = \int_{-\infty}^{\infty} \psi(X, \bar{Y}, Z)\, e^{-i\omega Z}\, dZ. \tag{5.13}$$

This reproduces (3.9$a-d$) effectively, however, with b^2 replaced by ω^2 in (3.9a) and b by $-i\omega$ in (3.9a–c). Hence all the analytical properties in (4.3)–(4.8 b) can be converted readily to this isolated-VG case (see also the next section).

If, additionally, the isolated VG is slowly varying in the spanwise direction then an analogue of (i) above applies. In particular, the streamwise scale downstream becomes elongated by a factor b^{-1}, where b^{-1} denotes the relatively long spanwise scale. Likewise, with fast spanwise variation present at a particular Z location, e.g. near a corner in the VG shape, an analogue of (ii) becomes relevant. The latter leads to a two-layer development over most of the VG, and beyond, at such spanwise locations, as in (5.7)–(5.12b).

6. For real VG shapes

To handle realistic VG shapes rather than the single-mode forms studied in §§4 and 5, we return to the series form (3.7) with (3.8). Thus the individual Fourier components of the solution such as those discussed in the previous two sections are now summed up computationally over a large number (N) of terms, giving the results in the following figures. These are described below, including further comments which cover the downstream behaviour and the most advantageous VG shapes, while parameterization and comparisons with experiments are presented in Appendix C.

6.1. *Triangular VGs*

A triangular VG has the shape function

$$f(X, Z) = \begin{cases} X & \text{for} \quad 0 < X < 1, |Z| < \hat{L}, \\ 0 & \text{otherwise}, \end{cases} \tag{6.1a, b}$$

where L is the maximum spanwise half-width and $\hat{L} = L(1-X)$. To aid the computational treatment, after some preliminary trials we decided to address a smoothed version of (6.1), namely

$$f(X, Z) = X\left\{\frac{X^2}{\epsilon_2^2 + X^2}\right\}\left\{\frac{(1-X)^2}{\epsilon_2^2 + (1-X)^2}\right\} g(Z) \tag{6.2a}$$

replacing (6.1a), with

$$g(Z) = \begin{cases} 1 \quad \text{for} \quad |Z| < \hat{L}_1 \\ \{1-(Z-\hat{L}_1)^2/(\hat{L}-\hat{L}_1)^2\}^2 \quad \text{for} \quad \hat{L}_1 < Z < \hat{L}, \\ \text{symmetric in } Z, \end{cases} \tag{6.2b}$$

$[\hat{L}_1 = (1-\epsilon_1)\hat{L}]$, as presented in figure 5. Here the fractions ϵ_1, ϵ_2 are usually taken as small. This version helps in the convergence of the Fourier series results, with the non-smoothed triangular shape of (6.1) being recovered in the limit of small ϵ_1, ϵ_2. We assume an array of VGs (6.2) (or (6.1)) spaced periodically in Z; the corresponding Fourier components $f_n(X)$ in (3.7) may then be worked out in the standard way; the

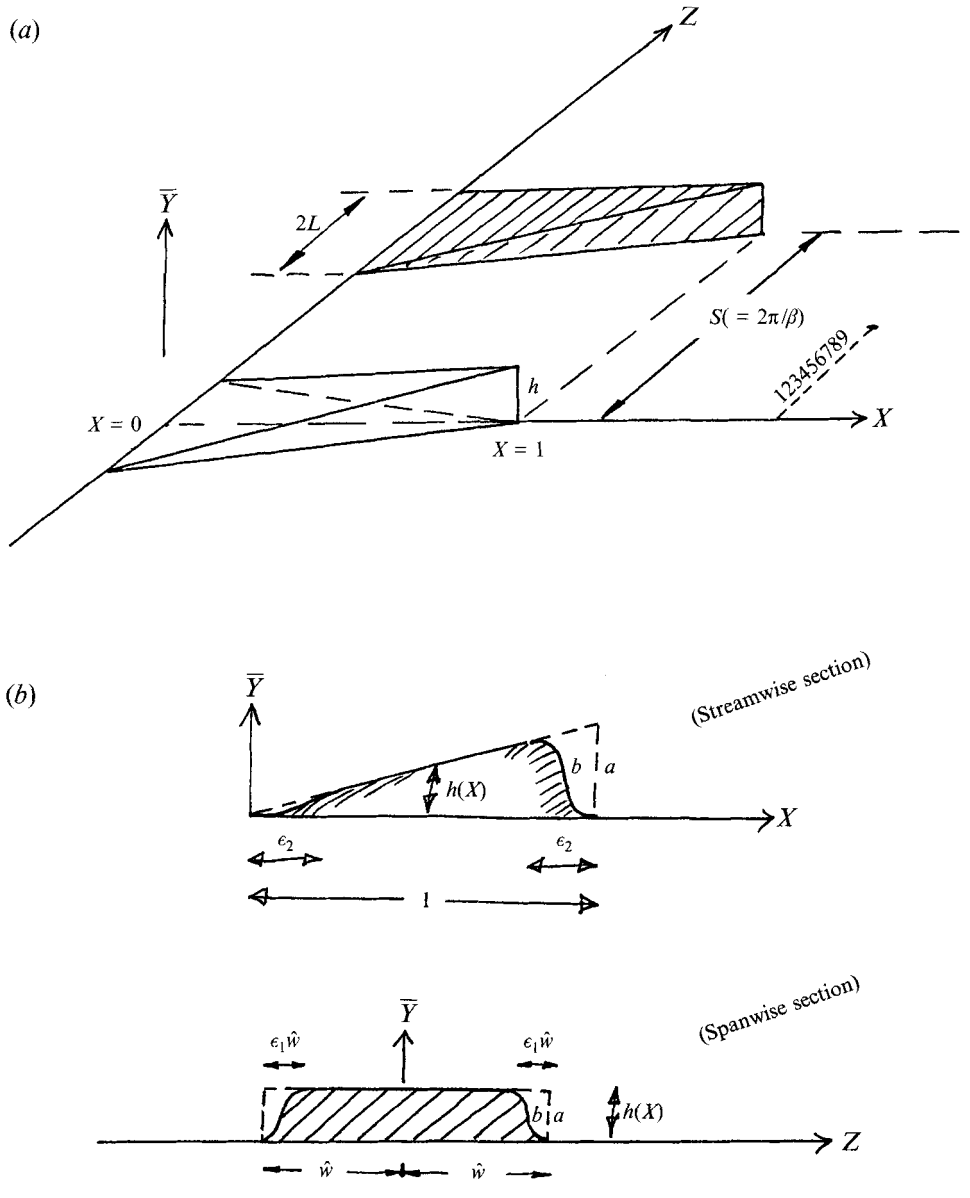

FIGURE 5. Sketch of (*a*) triangular and (*b*) smoothed VGs, and notation, including the Z-locations (1–9) of the results presented in figures 6–10 below. *a*: non-smoothed case; *b*: typically smoothed case.

computational method of §4 then provides the solution components ψ_n; and the real VG solution properties then follow on summation as in (3.8).

The results in figure 6 are for small values of the smoothing parameters ϵ_1, ϵ_2 in (6.2), and trends for the case (6.1) can be picked out as ϵ_1, say, is decreased. There is clearly still a significant loss of resolution in the computational results as the trailing edge ($X = 1$) of the VG is approached, in the form of wavelike oscillations in the streamwise direction. Nevertheless, the results for small ϵ_1, ϵ_2 values, combined with the grid-effect and geometry studies below, indicate well the solution response for triangular VGs. We note in particular the marked effects just off-centre (compare also §6.6, Appendix B)

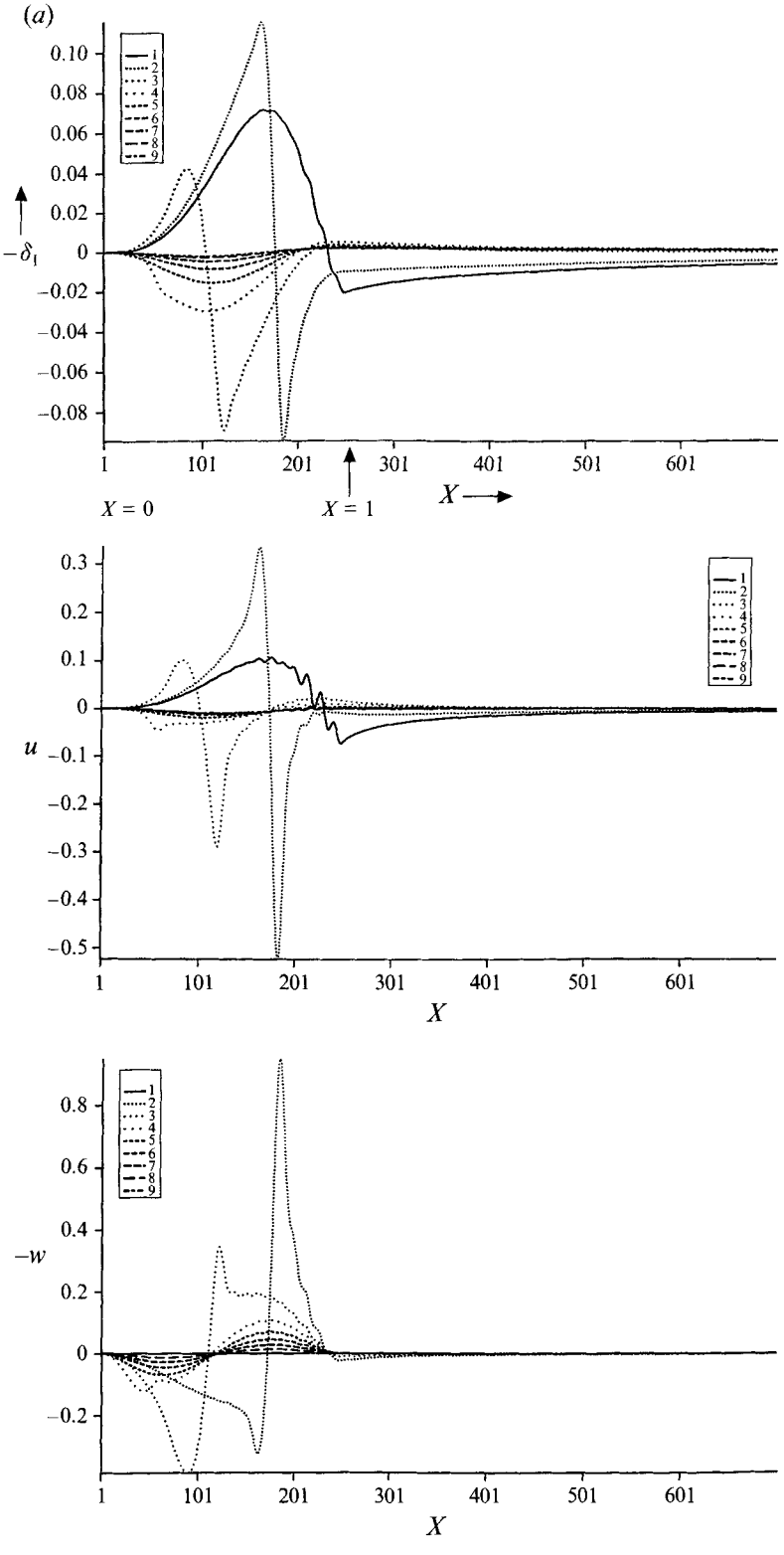

FIGURE 6(*a*). For caption see page 116.

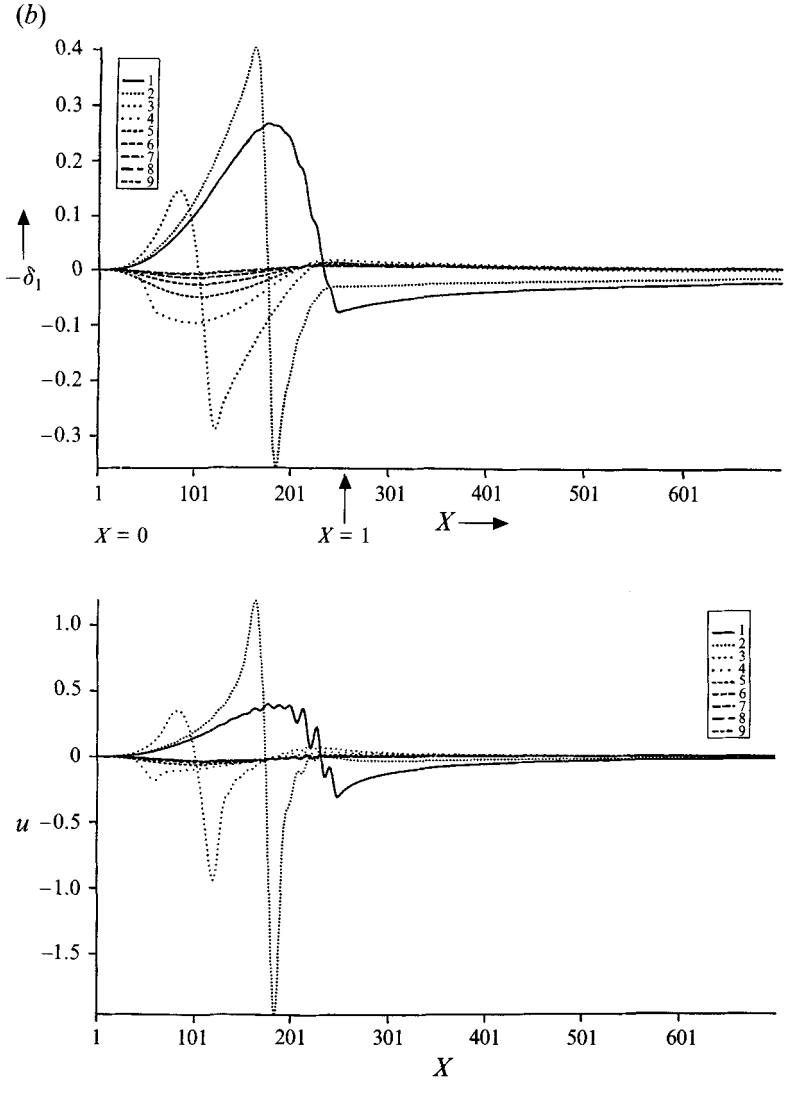

FIGURE 6(*b*). For caption see page 116.

near the 'end' of the VG for non-zero Z values, where (e.g.) the maximum displacement occurs. In contrast, there is hardly any effect from the VGs on the flow mid-way between the VGs (compare also §6.4 below).

6.2. *Moderately smoothed VGs*

These correspond to increased values of the smoothing parameters ϵ_1, ϵ_2, and results are shown in figure 7. On the computational side, there is improved resolution as expected. More significant in practical terms, however, is the reduction of off-centred effects (compared with §6.1), e.g. in displacement, surface velocity; this reduction is disadvantageous, as we see below in §6.6, even though it can be counterbalanced to some extent by increasing the volume or height of such a VG.

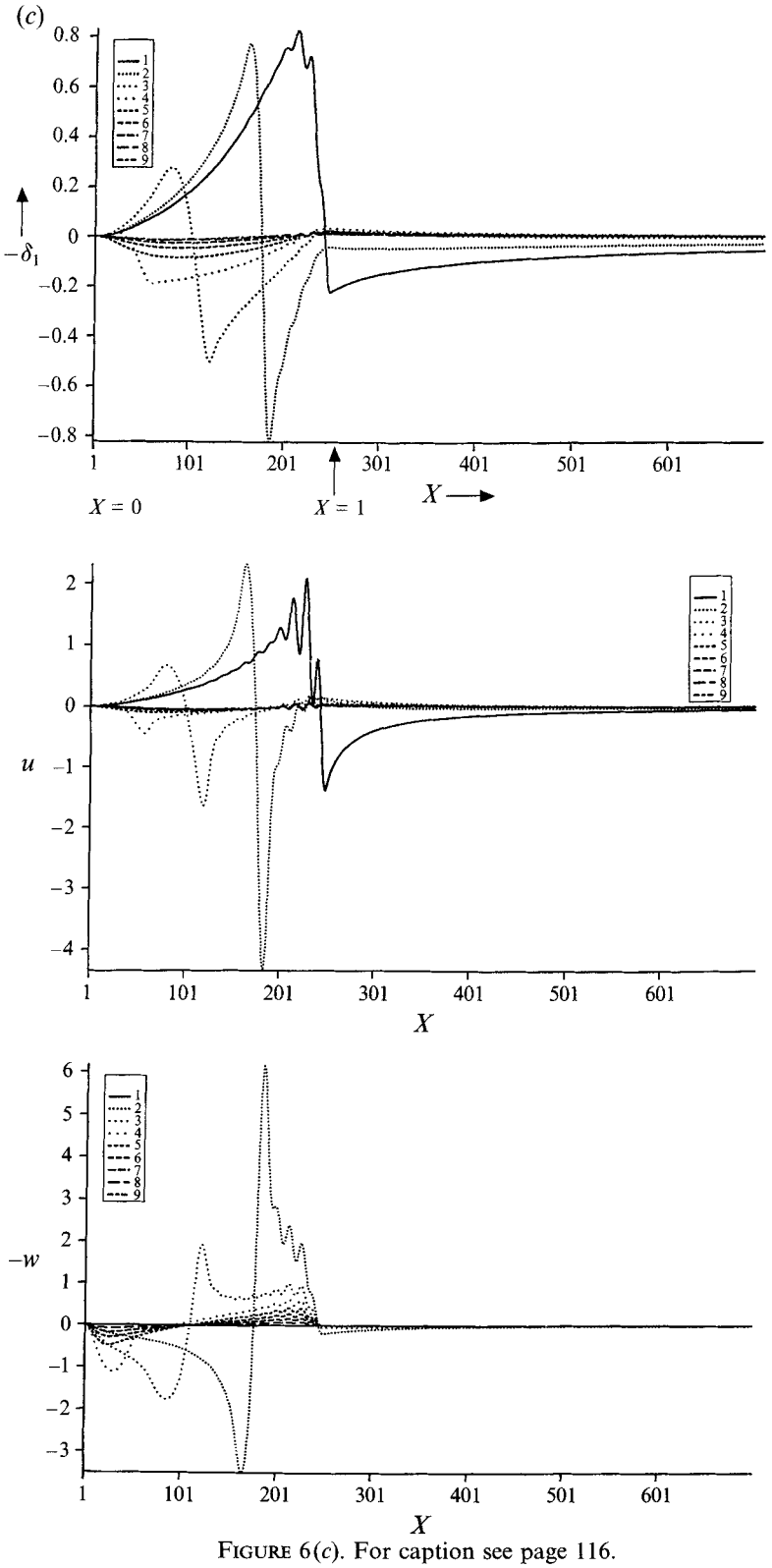

FIGURE 6(*c*). For caption see page 116.

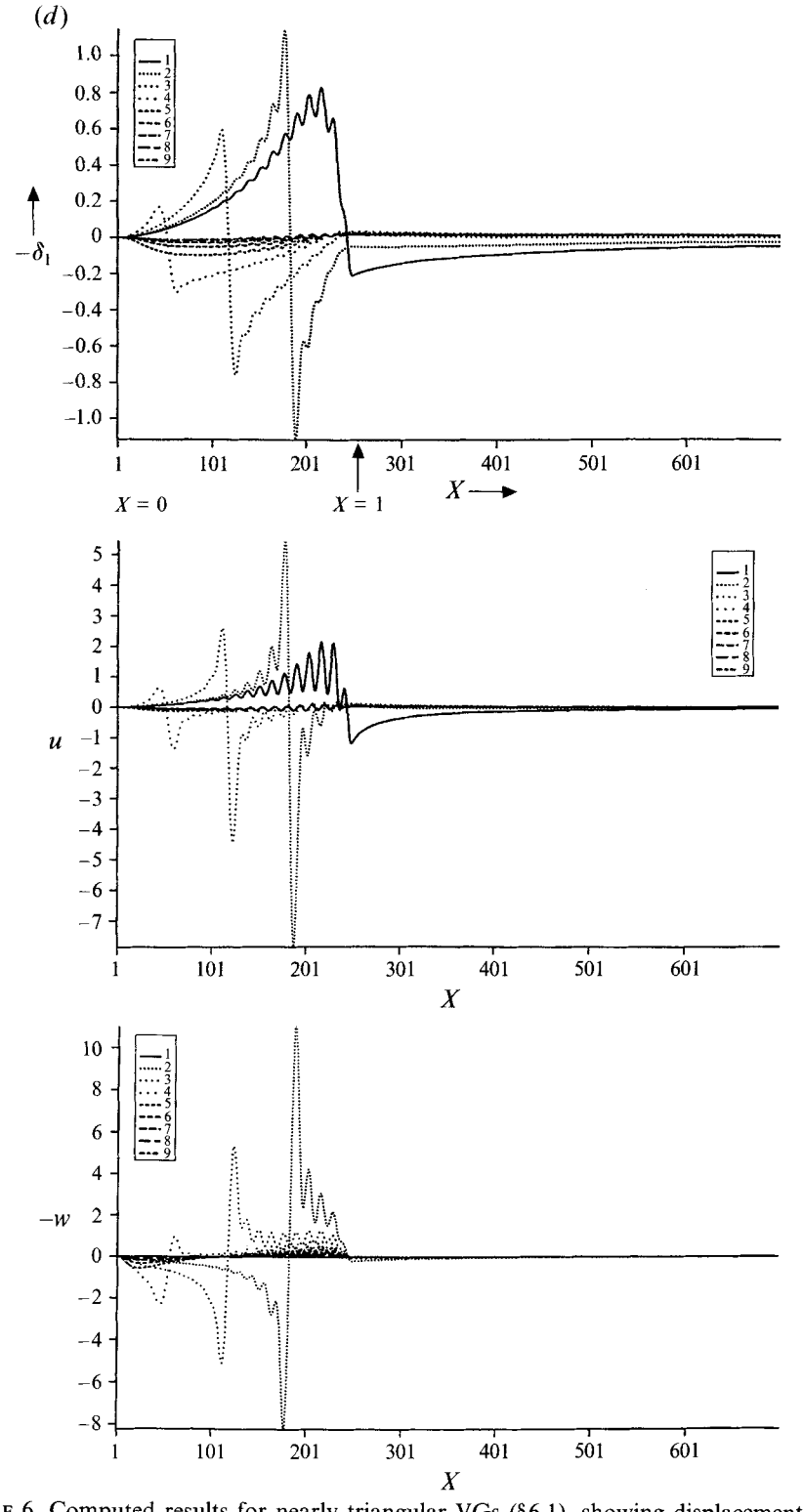

FIGURE 6. Computed results for nearly triangular VGs (§6.1), showing displacement effect δ_1 and surface velocities u_{11}, w_{11} at $\bar{Y} = 0$ (denoted u, w) for Z-locations 1–9 as marked in figure 5. The runs have (*a*) $(\epsilon_1, \epsilon_2) = (0.3, 0.6)$; (*b*) (0.3, 0.3); (*c*) (0.3, 0.1); (*d*) (0.1, 0.1). Scaled width $2L = \pi$ throughout. See also comparisons in figure 10.

6.3. *Completely smoothed VGs*

These have the value $\epsilon_1 = 1$ (figure 8) and are included partly for comparison with the above cases and partly to check against analysis as in §6.6 below. The trends of §§6.1 and 6.2 are continued here, i.e. the flow solution is generally milder and smoother, as comparisons with figures 6 and 7 show.

6.4. *Spanwise-packing effects*

Figure 9 shows the effects of increasing the spanwise packing or density, i.e. decreasing the spanwise period length $S\ (= 2\pi/\beta)$ of figure 5, while keeping the VG shape the same as in a previous figure. The results in figure 9 are most interesting in that increased packing clearly has a beneficial influence, in raising both the 'off-centredness' of the flow response (e.g. displacement, surface velocity) and the amplitude of that response (see also §6.6 below).

6.5 *Grid-distribution effects*

The accuracy of the above results was tested by altering the grid parameters, namely the step sizes ΔX, $\Delta \bar{Y}$, the upper edge value $\bar{Y}_\infty$ and the number N of Fourier terms taken. The results in the previous figures have the parameter values (0.004, 0.02, 16, 80) respectively, while the checks in figure 10 have various other combinations of the grid parameters as indicated in the captions. We should stress that except in some extreme cases the changes produced seem satisfactorily small, indicating quite high accuracy throughout. This is particularly so for all the smoother VG cases, for example those shown in figures 7–9. We present figures 6 and 10, however, deliberately to draw attention to the difficulties in extreme cases of nearly sharp VGs. Thus, the alterations due to halving ΔX, $\Delta \bar{Y}$, $\bar{Y}_\infty$ in figure 10(a, c, d) are tiny almost everywhere and virtually negligible in graphical terms: the results in figure 10(a, c, d) are hardly distinguishable from the corresponding ones in figures 7 and 6(c) in turn. Concerning the influence of the number of spanwise modes N on the other hand, while a comparison of figures 10(b) (where $N = 40$), and 6(c) ($N = 80$) for example shows agreement at positions away from the nearly sharp edges there are clearly difficulties near those edges. This is the main grid effect, as might be expected. The results still seem to imply that the oscillations present in the above figures are decaying, albeit slowly, as N is increased and the errors are confined near the sharp edges. Similar considerations apply to other quantities and other figures. In the extreme cases upon which figures 6 and 10 concentrate, then, many more than 80 modes are necessary for full resolution locally near the sharp edges. Nevertheless, the computed solutions appear to be fairly accurate even locally, as is supported by analysis based on §5(c) for the flow near the almost sharp trailing edge produced when ϵ_2 is small. The scaling there is $O(\epsilon_2)$ in terms of $X-1$, $\bar{Y}, Z$ and the analysis suggests the displacement correction δ_1 to be $f(x)\ln\epsilon_2$, to within a constant. The comparisons shown in figure 10(b) indicate that the $N = 40$, 80 results are in keeping with the analysis despite the slow convergence with respect to N. Moreover, the very existence of the distinct $O(\epsilon_2)$ sized zone near the almost sharp edge confirms that slow spectral convergence in N is to be expected.

6.6. *Comments on the results*

We take it that a reasonable (first) measure of the 'benefit' produced by a VG array is the strength of the main longitudinal vortices induced downstream, combined

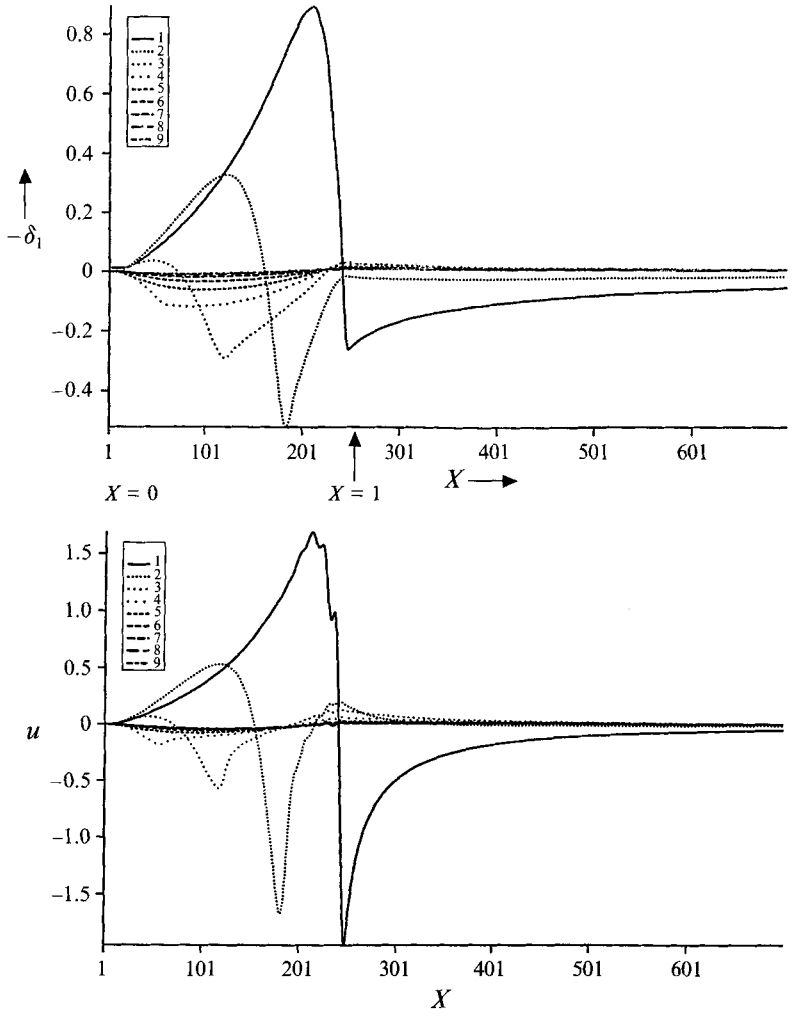

FIGURE 7. As figure 6 but for moderately smoothed VGs (§6.2). Here $(\epsilon_1, \epsilon_2) = (0.7, 0.1)$. See also comparisons in figure 10.

perhaps with a general reduction in the downstream flow displacement (as anticipated in §1). Based on such a measure, the results in §§6.1–6.4 imply fairly clearly that high benefit comes from a combination of

increased spanwise packing, (6.3)

increased VG volume, (6.4)

suitably non-smooth VG shapes, (6.5)

within certain limits.

For each of (6.3)–(6.5) increases the amplitude of the 'off-centredness' in the flow response (referred to in §§6.1–6.4) over the VG, and this off-centredness acts to drive the longitudinal vortex system as it develops downstream.

The same conclusion about the advantages of (6.3)–(6.5), by and large, is found from analysis of the flow solution far downstream, along the lines of (4.6*a–c*) and Appendix

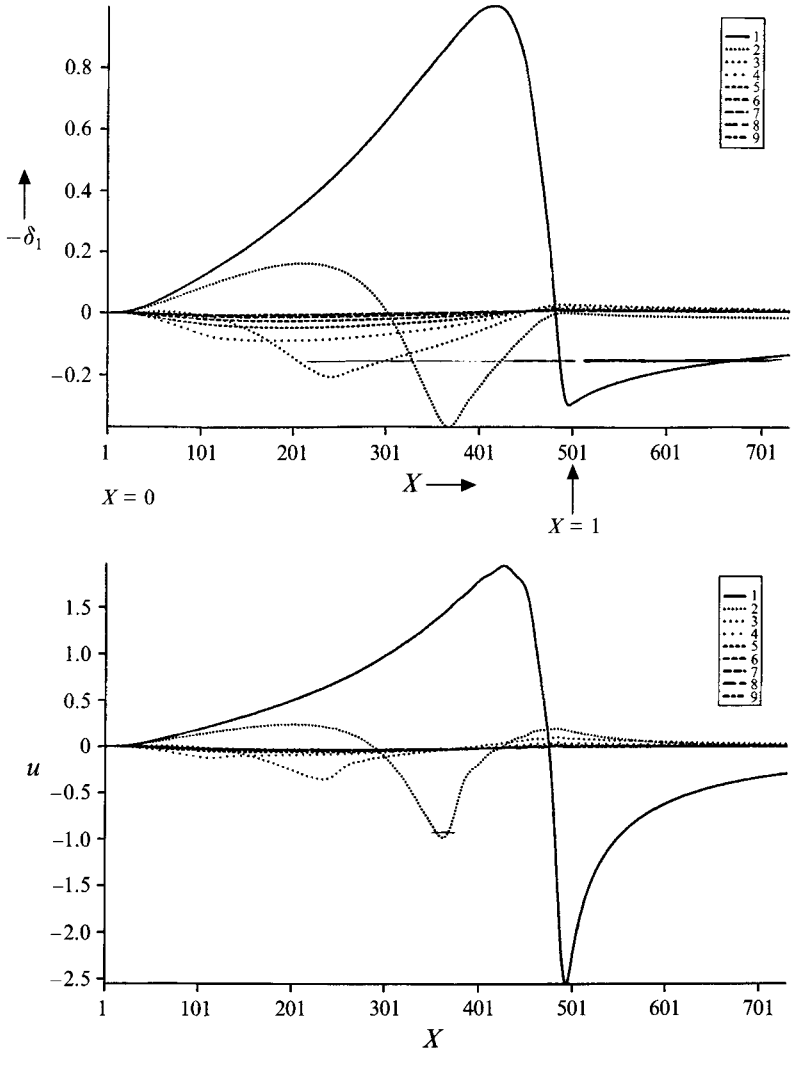

FIGURE 8. As figure 6 but for fully smoothed VGs (§6.3). Here $(\epsilon_1, \epsilon_2) = (1, 0.1)$.

A. Thus, using (A 1), (A 7) with (4.2*b*, *e*, *f*), we find for the displacement function in particular that

$$\delta_1 \sim \tfrac{1}{2} u_e A(Z) X^{-1}, \tag{6.6}$$

as $X \to \infty$, where $A(Z)$ is the net cross-plane area of the VGs, but with the mean value subtracted out,

$$A(Z) \equiv \int_0^\infty [f(X, Z) - f_{\text{mean}}(X)]\, \mathrm{d}X, \tag{6.7a}$$

$$f_{\text{mean}}(X) = S^{-1} \int_0^S f(X, Z)\, \mathrm{d}Z. \tag{6.7b}$$

The fact that $A(Z)$ has zero mean (spanwise) plays an important role, as we see below.

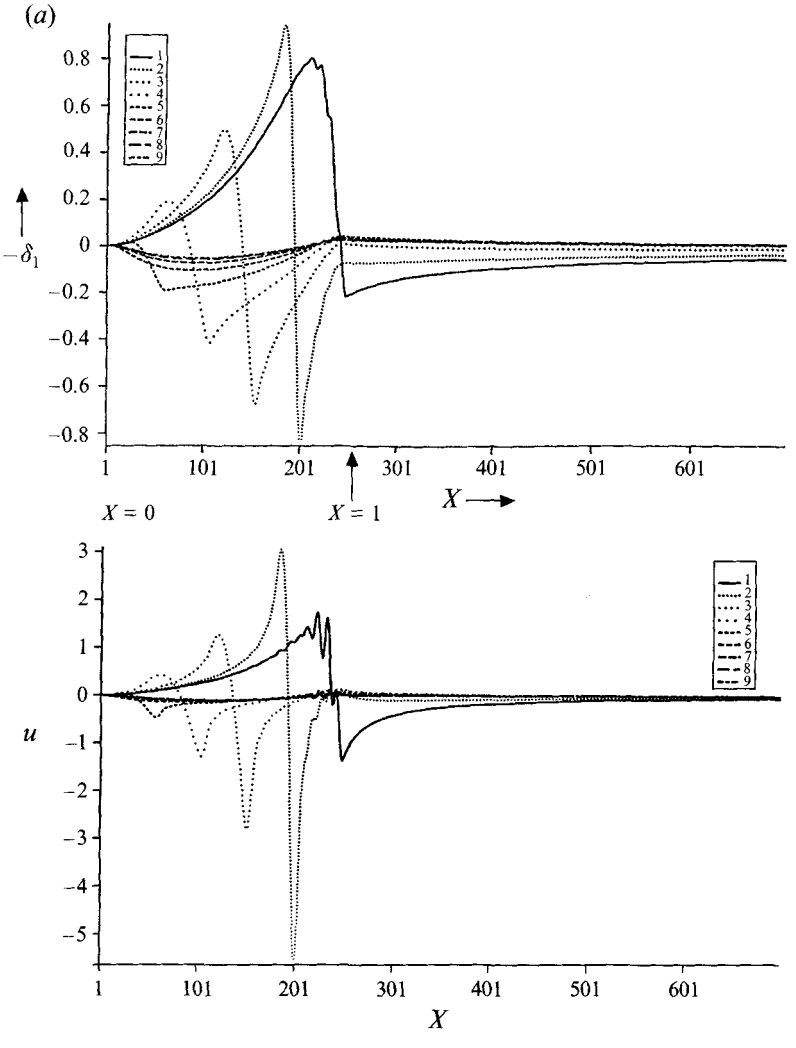

FIGURE 9(*a*). For caption see facing page.

In addition, the strength of the main (outer) longitudinal vortex system downstream is represented by $\Omega \equiv V_{11Z} - w_{11Y} = (\partial_Y^2 + \partial_Z^2)\psi$, while the vortex centres are located where ψ_Y, ψ_Z both vanish. Hence, it is found that the maximum vortex strength behaves downstream according to

$$\Omega \propto X^{-2}(\ln X)^{-1}\frac{\mathrm{d}A}{\mathrm{d}Z}, \tag{6.8a}$$

at the vortex centres which occur at the positions $Z = Z_{VC}$ where

$$A(Z_{VC}) = 0. \tag{6.8b}$$

Asymptotes similar to (6.6) and (6.8*a*) can be obtained for the other flow quantities of interest.

The analytical results (6.6), (6.8*a*, *b*) and similar ones for other quantities tend to

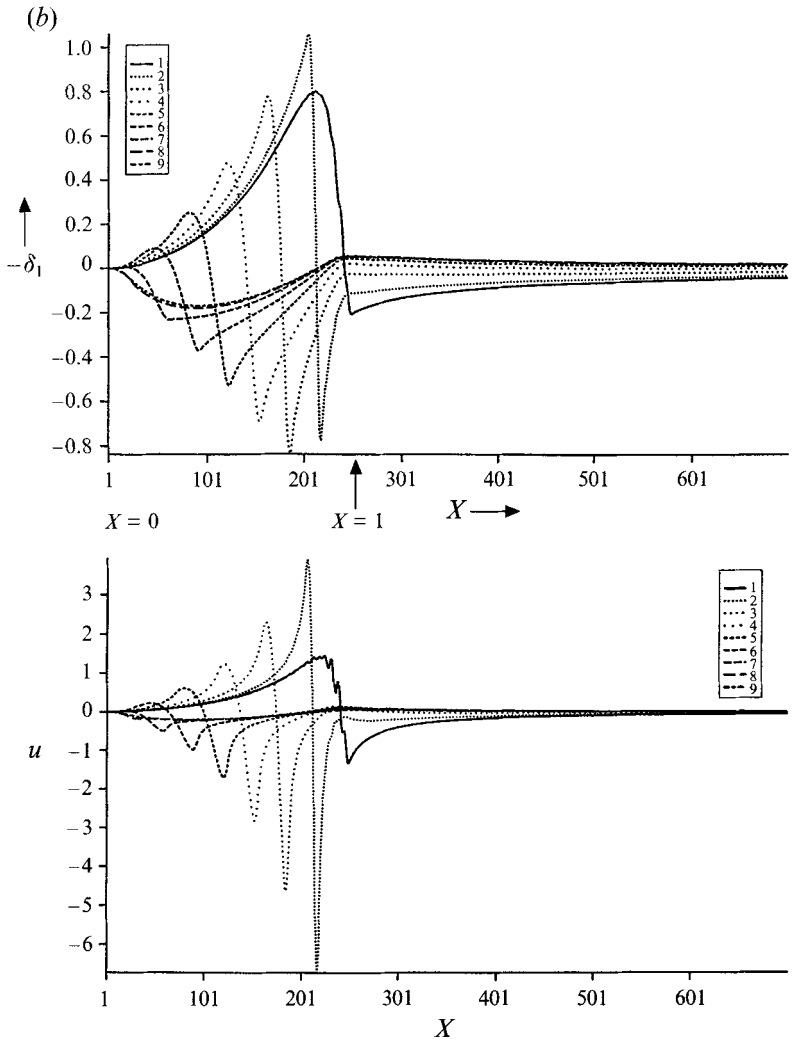

FIGURE 9. Computed results showing effects of spanwise packing (§6.4). Here $(\epsilon_1, \epsilon_2) = (0.3, 0.1)$, but (*a*) $S = \frac{3}{2}\pi$; (*b*) $S = \pi$ (whereas $S = 2\pi$ in all other results).

suggest that the benefit (defined earlier) is raised by, first, maximizing the mean contribution

$$\int_0^\infty f_{\text{mean}}(X)\,\mathrm{d}X, \tag{6.9}$$

and, secondly, increasing the slope of $A(Z)$ (generally, but more especially in-board, towards the centreline, and including the locations Z_{VC} of (6.8*b*)); see also figure 11. This is because maximizing (6.9) lowers $A(Z)$, and hence has the desirable effect of lowering the displacement (6.6), at most Z values, as well as decreasing Z_{VC} which then has the desirable effect of increasing the vorticity strength in (6.8*a*). Directly increasing the in-board slope $\mathrm{d}A/\mathrm{d}Z$ has a similar favourable effect. Further, the suggested increasing of (6.9) and/or the in-board slope of $A(Z)$ is achieved by applying (6.3)–(6.5); for (6.3) and (6.4) raise the value of (6.9) directly, while (6.4) and (6.5) can

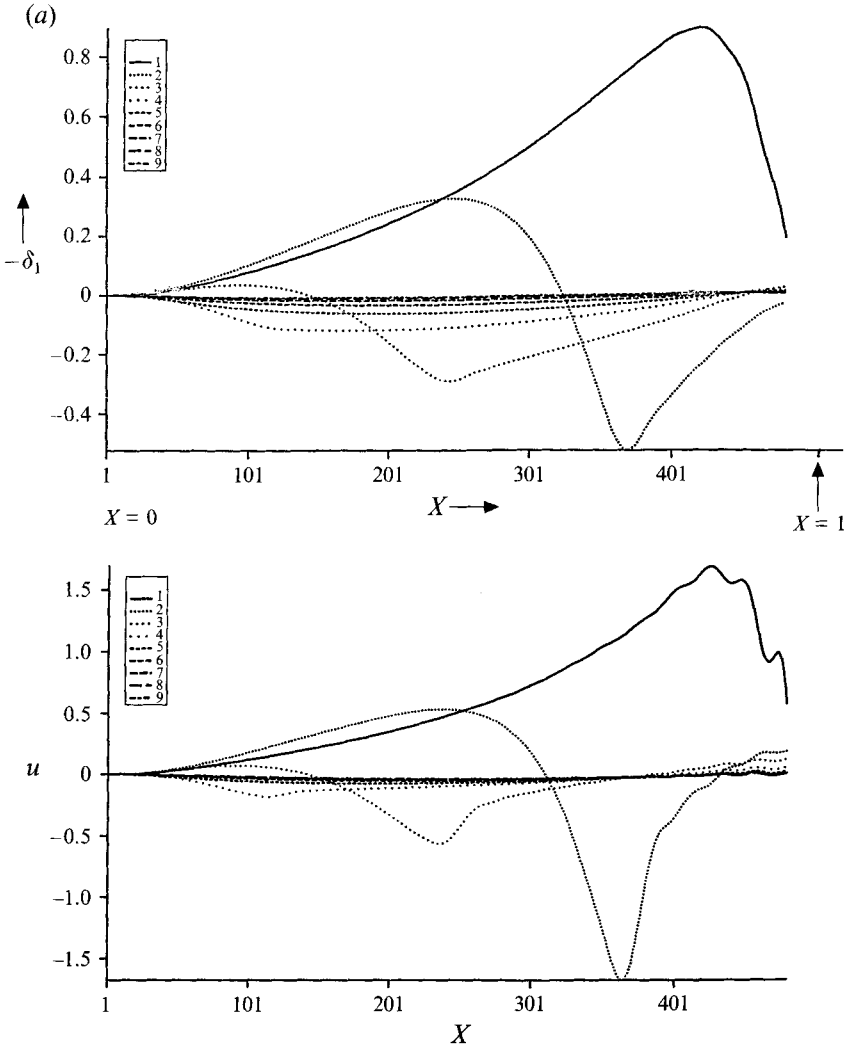

FIGURE 10(*a*). For caption see page 125.

raise the in-board values of dA/dZ directly. Examples illustrating these features are presented in figures 11 and 12 (where, to repeat, the edge of the boundary layer is strictly far outside the current $\bar{Y}$ range) and in Appendix B, where the triangular VG is addressed specifically.

So the advantages of (6.3)–(6.5) for VG arrays appear to be confirmed by both the earlier computations and the downstream analysis. The latter has more universality and flexibility, however, e.g. in indicating the crucial part played by the integral property $A(Z)$ in (6.8*a*), and this leads to the recommendations made in the next section.

7. Suggestions on VG shapes and distributions, and further comments

The suggestions/recommendations below on VG shapes and arrays follow straight on from §6, and especially from the three beneficial properties identified in (6.3)–(6.5)

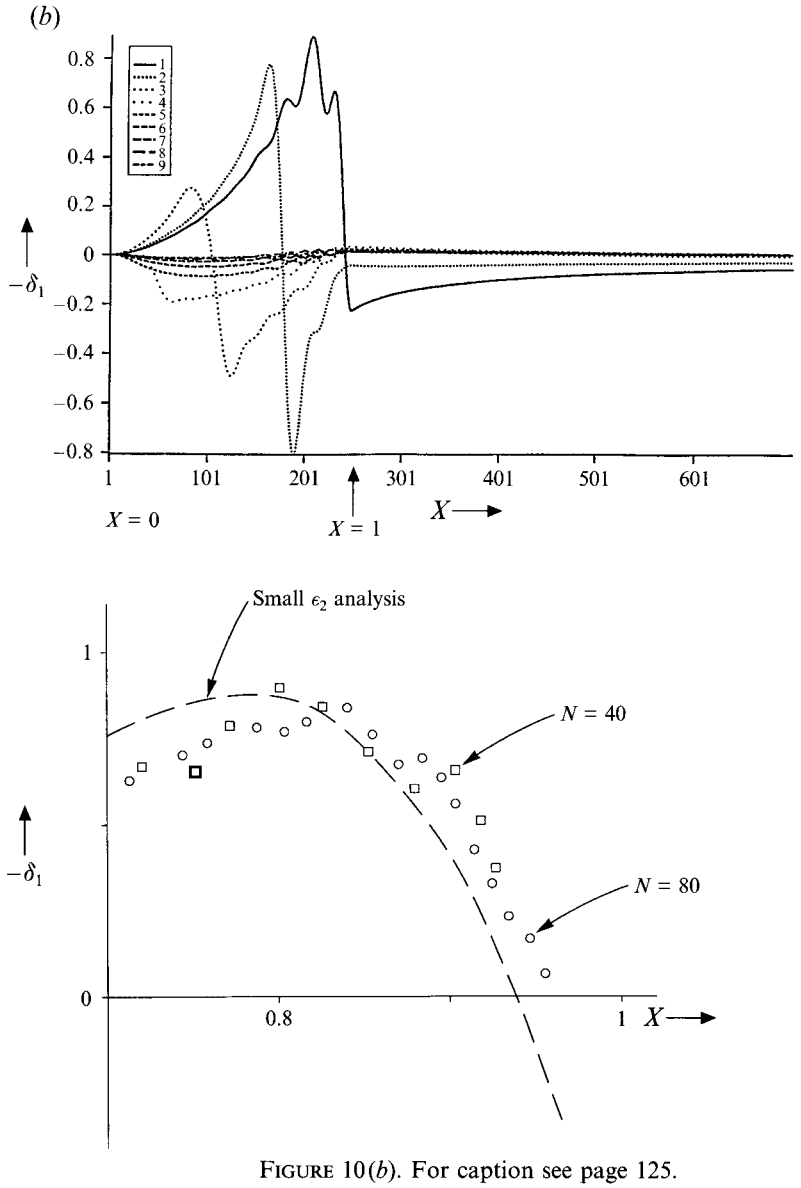

FIGURE 10(*b*). For caption see page 125.

(or (1.1)–(1.3)) and the formulae involving the net area function $A(Z)$ in (6.6), (6.8).

First, (6.3) suggests using spanwise distributions of VGs very close to or even touching each other.

Secondly, (6.4) is perhaps best achieved by elongating the VG streamwise (on account also of (6.3) and (6.5)).

Thirdly, (6.5) may be applied by adding on a spanwise pinched contribution to an existing triangular VG (or to a similar shape), or even mounting a slender triangular VG on top.

These suggestions are illustrated in figure 12, which in addition shows results for a particular shape approximating to the type envisaged in the previous paragraph. The three suggestions above are still tentative of course (e.g. the pinched contribution if

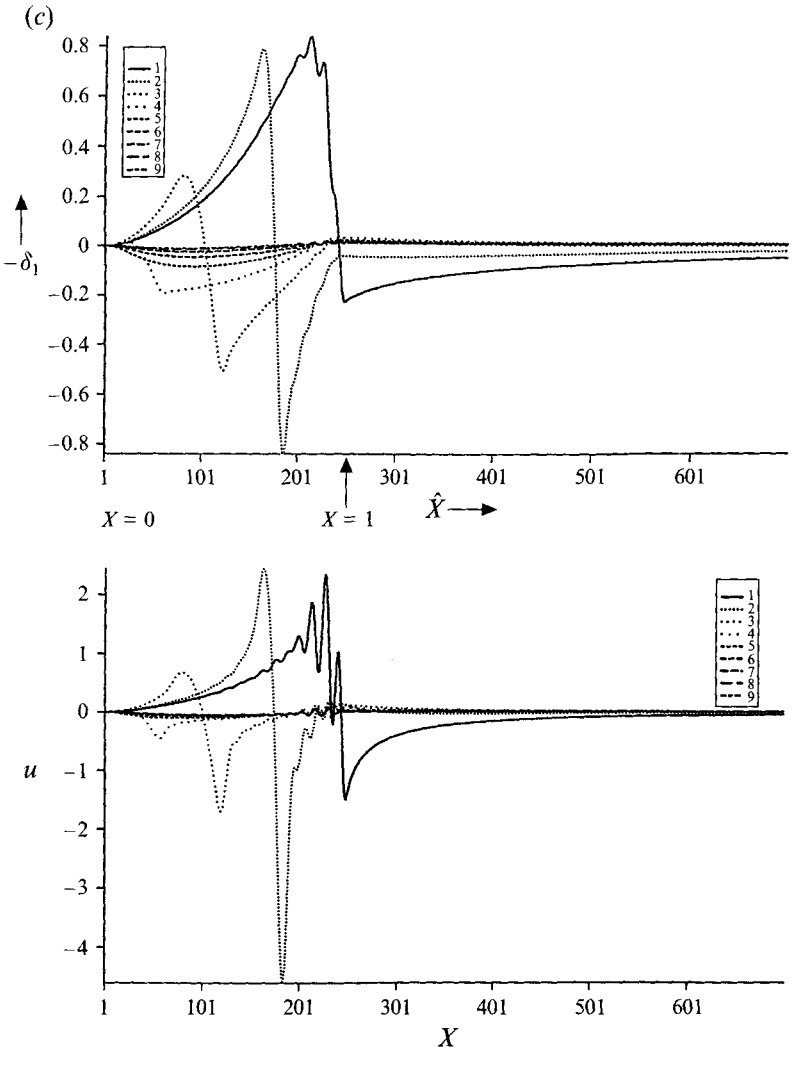

FIGURE 10(*c*). For caption see facing page.

taken to an extreme (as with a vane-type VG) would lie outside the scope of the present theory) and experimental or fully computational studies (some underway by D. McCormick & T. Barber) could help in checking or comparing with the results in figures 6–12 as well as with the three suggestions just described; see also, however, the comparisons and parameter groups in Appendix C.

Next, it is worth noting certain other VG arrangements that have been used experimentally. These are the plough shape, the doublet arrangement, and the staggered array. The first of these still has a triangular VG shape for instance but pointed upstream; according to the theory the net effect far downstream is not altered significantly from that for the original triangular case. The second has an extra VG array immediately downstream of a first array; here the net effect far downstream is doubled. The third, the staggered array, produces little alteration far downstream. Thus, according to the theory at least, the doublet arrangement (which may be likened

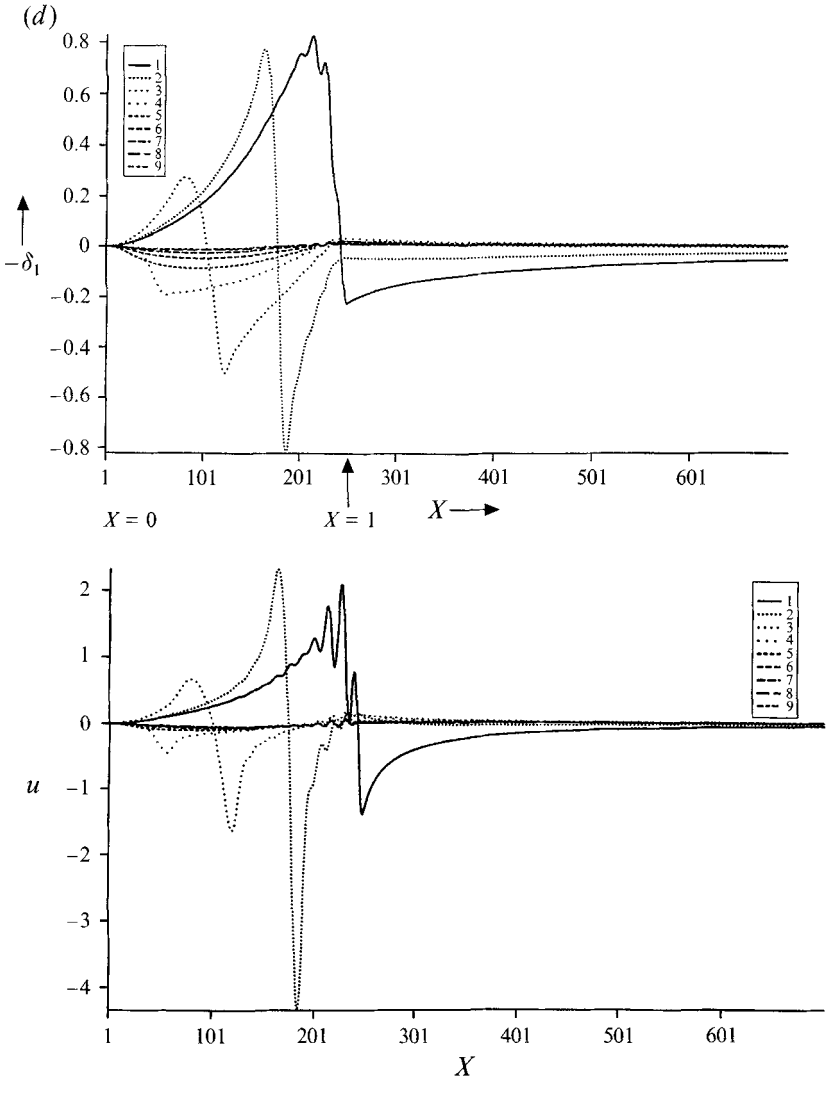

FIGURE 10. Grid-size effects on the computed results (§6.5). Here figure 10(*a*) is as figure 7 but ΔX halved. Figure 10(*b*) is as figure 6(*c*) but N halved, and a comparison is included between the $N = 40$, 80 results and analysis, for ϵ_2 small. Figure 10(*c*) is as in figure 6(*c*) but $\Delta \bar{Y}$ halved. Figure 10(*d*) is as figure 6(*c*) but $\bar{Y}_\infty$ halved.

in effect to the recommendation above associated with (6.4)) is likely to be the only advantageous one among these particular three arrangements.

Other, generally lesser, points for the record may be listed as follows.

(i) The more positive aspects of the theory have been stated earlier, e.g. its incorporation of the turbulent stresses, the logarithmic profile present, the flexibility of the formulae e.g. in suggesting designs of VGs (see above), the capturing of major parameters. There are negative aspects also, however, as stated earlier and these merit further study eventually; see also (v) and (vi) below.

(ii) Concerning §6.6, the spanwise surface velocity far downstream also depends on

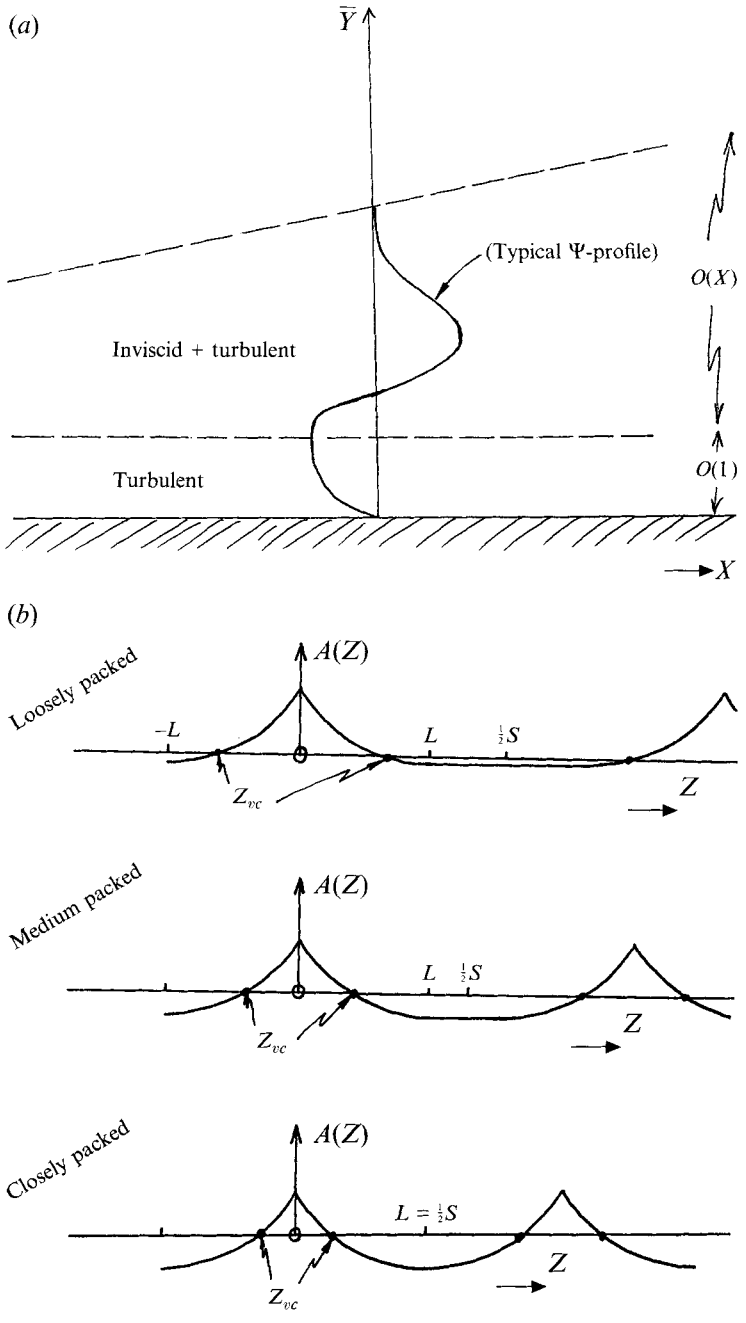

FIGURE 11. (*a*) Downstream flow structure (see Appendix A). (*b*) The net area function $A(Z)$, for triangular VGs, including the effect of varying the spanwise packing (see §6.6 and Appendix B).

$A(Z)$ but in the form of a Cauchy–Hilbert integral, in contrast with the properties addressed in §6.6.

(iii) Two streamwise vortex systems are produced downstream, as mentioned earlier: see also Appendix A, and in particular the prediction (A 14) for the centre of the outer vortex system produced by any VG array.

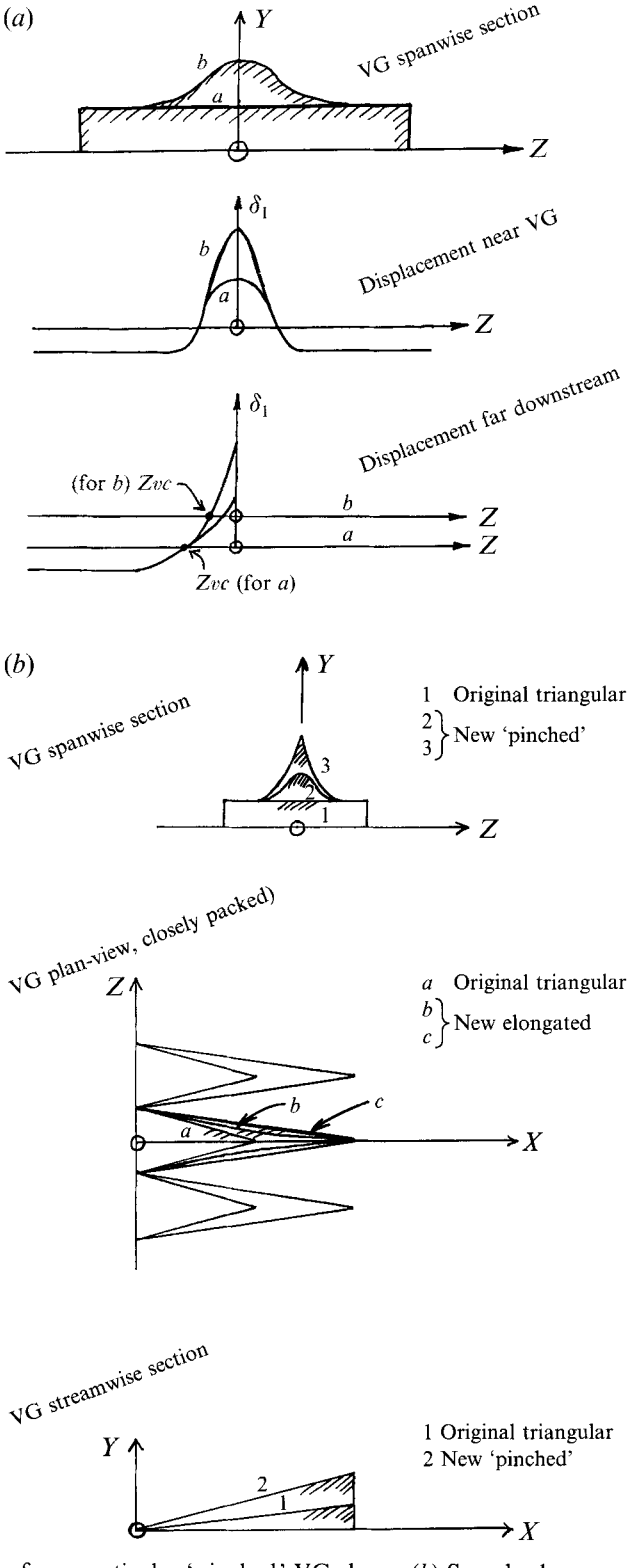

FIGURE 12. (*a*) Results for a particular 'pinched' VG shape. (*b*) Sample shape suggestions (see §§6.6 and 7).

(iv) It is interesting to note that the most beneficial spacing for a triangular VG, according to Appendix B, has S/s equal to approximately 2.4 far downstream, compared with Pearcey's (1961) value of approximately 4 (for generally higher-profile VGs). Again, the results in figures 6–10 appear to yield S/s values in the range 2–6 approximately (Here s is the spanwise distance between the centres of the longitudinal vortices trailing a VG, at some streamwise station; we take that to refer to the outer pair of longitudinal vortices).

(v) Further work is required on the influence of nonlinear effects, separation from the VG, the boundary-layer upper edge, and on other possible VG distributions, depending perhaps on further experimental findings. Preliminary ideas on these features and those in (vi) below are under consideration.

(vi) Many variants and extensions of the current theory are possible in principle (some of which are mentioned in §§3–6), e.g. for other VG arrays, for the flow much further downstream, for corners on VGs inducing separations in the form of vortex sheets, for incoming boundary layers with cross-flow, for compressibility effects, for pressure–displacement interaction, and for other turbulence models.

However, the suggestions/recommendations given at the start of this section are felt to be the most useful points.

Thanks are due to Duane McCormick, Tom Barber, Bob Patterson and the late Jon Mounts, for discussions, to United Technologies Research Center for support (this work appeared originally as a UTRC report, 1992, no. 92-8), to SERC, UK and the University of London Computer Centre for computer facilities, to Andrew Walton for processing assistance, and to the referees for their interesting comments.

Appendix A. The behaviour far downstream

At large positive X far downstream of the VG the flow solution acquires a two-layered structure, as follows.

The inner layer occurs where $\bar{Y}$ (which equals Y since here F is zero) has $O(1)$ values and the streamfunction expands in the form

$$\Psi = X^{-2}L^{-2}[\psi_0(\bar{Y}) + L^{-1}\psi_1(\bar{Y}) + \ldots], \tag{A 1}$$

with $L \equiv \ln X$. Substitution into (3.9a) shows the flow here to be turbulent-stress-dominated, such that at leading order

$$-b^2\bar{Y}\psi_0' + \bar{Y}\psi_0''' + \psi_0'' = d_0, \tag{A 2}$$

where d_0 is an unknown constant. Hence $g_0 \equiv \psi_0'\hat{d}_0^{-1}$ is governed by

$$\hat{y}\,\mathrm{d}^2 g_0/\mathrm{d}\hat{y}^2 + \mathrm{d}g_0/\mathrm{d}\hat{y} - \hat{y}g_0 = 1, \tag{A 3}$$

with $\hat{y} = b\bar{Y}$, $\hat{d}_0 = b^{-1}d_0$. The solution satisfying the no-logarithm constraint (3.9d) as $\hat{y} \to 0$ and no exponential growth as $\hat{y} \to \infty$ is unique,

$$g_0 = I_0(\hat{y})\,H(\hat{y}), \quad H(\hat{y}) = \int_\infty^{\hat{y}} \tilde{y}^{-1} I_0^{-2}(\tilde{y}) \left\{ \int_0^{\tilde{y}} I_0(\tilde{\tilde{y}})\,\mathrm{d}\tilde{\tilde{y}} \right\} \mathrm{d}\tilde{y}. \tag{A 4}$$

Therefore we have, for $\bar{Y}$ large,

$$\psi_0 \sim -\hat{d}_0 \ln \bar{Y} + \hat{e}_0, \tag{A 5}$$

$$\psi_1 \sim -\hat{d}_1 \ln \bar{Y} + \hat{e}_1, \tag{A 6}$$

where the constant $\hat{e}_0$ is given by an integral of (A 4), and (A 6) follows from similar analysis.

The outer layer then has $\bar{Y}$ larger, of order X, with $\bar{Y} = X\eta$ and

$$\Psi = X^{-2}L^{-1}[\phi_0(\eta) + L^{-1}\phi_1(\eta) + \ldots]. \tag{A 7}$$

Here (3.9*a*) shows that an inertia–stress balance holds, giving

$$2\phi_0 + \eta\phi_0' = -(\eta\phi_0')', \tag{A 8}$$

$$2\phi_1 + \eta\phi_1' + \phi_0 = -(\eta\phi_1')', \tag{A 9}$$

for the first two orders. These equations are subject to the constraints

$$\phi_0 \to -\hat{d}_0, \quad \phi_1 \sim -\hat{d}_0 \ln\eta + \hat{e}_0 - \hat{d}_1, \quad \text{as} \quad \eta \to 0, \tag{A 10}$$

$$\phi_0, \phi_1 \to 0 \quad \text{exponentially as} \quad \eta \to \infty, \tag{A 11}$$

to match with (A 5) and (A 6) and to satisfy (3.9*c*) in turn. The solution of (A 8) is then

$$\phi_0 = C_0(1-\eta)\mathrm{e}^{-\eta} + C_2\mathrm{e}^{-\eta}(\eta-1)\int_1^\eta \mathrm{e}^{\eta}\eta^{-1}(\eta-1)^{-2}\,\mathrm{d}\eta, \tag{A 12}$$

formally, where the constraints in (A 10) and (A 11) require the values $C_0 = -\hat{d}_0, C_2 = 0$. Hence, this far-downstream description appears to be self-consistent, and further terms in (A 1) and (A 7) can be determined at will.

The constant $\hat{d}_0$ (or d_0) remains arbitrary as far as the large-X analysis alone is concerned. In the nonlinear problem of §2, for which the present two-layer form still applies far downstream, $\hat{d}_0$ probably cannot be specified in advance. In the linear case, however, the working in §4 indicates the value

$$\hat{d}_0 = -u_e a\pi[2g_0(0)]^{-1}. \tag{A 13}$$

Again, the asymptotes (4.6*a–c*), which can be derived straight from (4.5*a–c*), are all in keeping with the description (A 1)–(A 12), and the leading-order stream-function profile implied by combining (A 1)–(A 5) with (A 7)–(A 12) is as displayed in figure 11(*a*). This verifies the occurrence of a double vortex pattern downstream (see also figure 2), since the Ψ profile has both a maximum and a minimum value with respect to $\bar{Y}$; these values define the positions of the longitudinal vortex centres lying along $Z = \pi/(2b)$, one being at just above $O(1)$ height in $\bar{Y}$ and the other at $O(X)$ height, within the outer layer.

Summation of the above results, for different values of $b = n\beta$, leads readily to the asymptotes for realistic VG shapes as quoted in (6.6)–(6.8*b*). We observe that in (6.7*a*) the mean value is subtracted in view of the third comment just prior to (3.10*a*), i.e. the mean flow or two-dimensional component makes no contribution. The vortex strength Ω quoted in (6.8*a*) concerns the outer longitudinal vortices and follows from (A 7)ff. In addition, the height of these vortices is given by

$$\bar{Y}_{VC} = 2X \quad \text{far downstream}, \tag{A 14}$$

for any VG distribution, because of (A 7) and (A 12).

Appendix B. Downstream response for triangular VGs

For the triangular shaped VG, defined in (6.1*a*, *b*), the net-area function $A(Z)$ which controls the far-downstream response (see Appendix A) is given by

$$A(Z) = \begin{cases} \dfrac{1}{2}\left(1 - \dfrac{|Z|}{L}\right)^2 - \dfrac{L}{3S} & \text{for} \quad |Z| < L, \qquad \text{(B 1)} \\[2ex] -\dfrac{L}{3S} & \text{for} \quad L < |Z| < \tfrac{1}{2}S, \qquad \text{(B 2)} \end{cases}$$

from application of (6.7*a*, *b*), where S is the spacing as shown in figure 5. The vortex centres far downstream are therefore located at

$$Z_{VC} = \pm L\left\{1-\left(\frac{2L}{3S}\right)^{\frac{1}{2}}\right\}, \tag{B 3}$$

from (6.8*b*). The vortex strengths on the other hand are given by the slopes $\mathrm{d}A/\mathrm{d}Z$ at the locations (B 3), from (6.8*a*), and these slopes increase in magnitude monotonically as $|Z_{VC}|$ decreases, i.e. as S decreases. The maximum vortex strength possible occurs in fact for the case of closest possible packing, where $S \to 2L$ and so $|Z_{VC}| \to L(1-3^{-\frac{1}{2}})$. In this case $s = 2|Z_{VC}|$ is $(1-3^{-\frac{1}{2}})$ times S, i.e. S/s is approximately 2.4 as quoted in §7.

Figure 11(*b*) illustrates (B 1)–(B 3) and the beneficial effects of closer packing (as in the suggestion (6.3)).

The results (B 1)–(B 3) can also be used to provide support for the suggestions (6.4) and (6.5), in particular from considering the benefit of placing a (spanwise) thinner VG on top of the original; for this also acts to decrease $|Z_{VC}|$ and increase the downstream vortex strengths (see also figure 12).

Appendix C. Comparisons with experiments, and parameter groups

Here we describe comparisons with experiments first and then parameter groupings suggested by the theory.

First, there are a number of points of agreement between the theoretical predictions and recent experimental results, kindly supplied to the author by D. McCormick, for low-profile triangular and plough VGs. These are summarized below.

(*a*) The spanwise *positions of the vortex centres*, downstream of the VGs, are found experimentally to be not far from the positions where the three-dimensional displacement thickness equals its original (baseline two-dimensional) value. This is in line with (6.8*b*) (see also figures 11 and 12).

(*b*) The three-dimensional displacement thickness in the experiments is approximately proportional to the momentum thickness, so that the *shape factor* is little altered. This agrees with the theory.

(*c*) The spanwise *mean of the three-dimensional displacement thickness* differs little experimentally from the baseline two-dimensional values (the typical difference is about 6% of the maximum deviation), in keeping with (6.6) and (6.7*a*).

(*d*) The measured *vortex strength* increases monotonically with the local displacement slope, in line with (6.8*a*).

(*e*) The experimental results for the *displacement- and momentum-thickness shapes* downstream, in the cross-plane, are broadly consistent with the theory, e.g. in (6.6), (6.7*a*, *b*) and figures 11 and 12.

(*f*) The theory predicts the *vortex-centre heights* approach the curve (A 14) downstream, which, allowing for (2.10), predicts a slope $\mathrm{d}y^*/\mathrm{d}y^*$ of $2a_1\Delta$, giving the value 0.0636 in one typical experimental run. The corresponding experimental slope is in the range 0.04–0.08, which seems in fair agreement.

Secondly, the theory indicates appropriate parameter groups, suggesting plotting of results as follows (with * denoting dimensional quantities).

Vortex centres: $(y^*, z^*)\,u_\infty^*/(u_\tau^*\,l^*)$ *vs.* x^*/l^*.

Velocity profiles: $(u_e^*-u^*,\ v^*,\ w^*)/u_\tau^*$ *vs.* $(x^*,\ y^*(u_\infty^*/u_\tau^*),\ z^*(u_\infty^*/u_\tau^*))/l^*$.

VG shape: $F^*u_\infty^*/u_\tau^*\,l^*$.

Streamwise vorticity: $(\partial v^*/\partial z^*-\partial w^*/\partial y^*)\,l^*/u_\infty^*$.

Here we recall that l^* is the VG length, u_∞^* is the local free-stream speed, and u_τ^* is the wall friction velocity.

REFERENCES

BUSH, W. B. & FENDELL, F. E. 1972 *J. Fluid Mech.* **56**, 657–668.

CEBECI, T. & SMITH, A. M. O. 1974 *Analysis of Turbulent Boundary Layers*. Academic.

CHIMA, R. V. & YOKOTA, J. W. 1989 *AIAA J.* **28** (5), 798–804.

DEGANI, A. T., SMITH, F. T. & WALKER, J. D. A. 1992 *J. Fluid Mech.* **234**, 329–360.

ESMAILI, H. & PIOMELLI, U. 1992 *AIAA paper* 92–0552.

FREESTONE, M. M., E.S.D.U. 1991/2 *Transonic Aerodynamic Committee papers* T729, T732, T733.

MCCORMICK, D. C. 1992 *AIAA paper* no. 92–0064.

MELLOR, G. L. 1972 *Intl J. Engng Sci.* **10**, 851–873.

MOUNTS, J. S. & BARBER, T. J. 1992 *AIAA paper* 92–0751.

NEISH, A. & SMITH, F. T. 1988 *J. Engng Maths* **22**, 15–42.

NEISH, A. & SMITH, F. T. 1992 *J. Fluid Mech.* **241**, 443–467.

PEARCEY, H. H. 1961 *Shock-Induced Separation and its Prevention by Design and Boundary Layer Control*, Part IV of *Boundary Layer and Flow Control*, ed. G. V. Lachman.

SCHUBAUER, G. B. & SPANGENBERG, W. G. 1960 *J. Fluid Mech.* **8**, 10–32.

VATSA, V. N. & WEDAN, B. W. 1988 *AIAA paper* 88–0102.